UNIVERSIDADE FEDERAL DE SÃO CARLOS

CENTRO DE CIÊNCIAS EXATAS E DE TECNOLOGIA

DEPARTAMENTO DE QUÍMICA

BORON-DOPED DIAMOND AS A POSSIBLE PEMFC ELECTROCATALYST SUPPORT MATERIAL

SAMUEL HENRIQUE MATTOSO

SÃO CARLOS – SP

2020

BORON-DOPED DIAMOND AS A POSSIBLE PEMFC ELECTROCATALYST SUPPORT MATERIAL

Trabalho de Conclusão de Curso apresentado ao Departamento de Química da Universidade Federal de São Carlos, para obtenção do título de bacharel em Química.

Orientador: Prof. Dr. Romeu Cardozo Rocha Filho

São Carlos – SP

2020

RESUMO

Células a combustível de membrana trocadora de prótons (PEMFCs) são candidatas promissoras para a conversão verde de hidrogênio em energia elétrica. Um problema considerável obstruindo a implementação em larga escala de PEMFCs é a durabilidade inadequada dos materiais componentes, como a degradação da camada eletrocatalítica suportada. Negros de fumo (CB), como Vulcan XC-72, são comumente usados como o suporte de carbono, contudo a sua estabilidade é limitante para o uso prolongado de PEMFCs. CB no catodo é oxidado na ciclagem de liga e desliga da PEMFC, desprendendo nanopartículas de Pt e formando aglomerados, levando a uma queda de desempenho. Essa degradação é devido aos potenciais elevados causados por escassez de combustível e à taxa de corrosão acelerada induzida pelos catalisadores de Pt. Diamante dopado com boro (BDD) possui propriedades interessantes, como alta estabilidade química e térmica, o que o faz um candidato como material de suporte de eletrocatalisador de PEMFC. O método mais comum para a produção de BDD é a deposição química em fase de vapor, pois é eficiente no controle de dopagem e também produz diamante com características consistentes. As propriedades físico-químicas e eletroquímicas do BDD são afetadas pela quantidade de carbono não diamante (NDC) presente na matriz do diamante, pelo tamanho de grão e pela dopagem de boro. Todas essas características são controladas pelas condições de CVD que são utilizadas, como concentração dos gases da fonte e pressão/potência de deposição. BDD pode ser sintetizado como um filme ou um pó, sendo que pós são mais procurados para aplicações em energia devido às suas maiores áreas específicas. Partículas de BDD podem ser sintetizadas através de um método *core-shell*, no qual um substrato em pó, como nanodiamante ou carbono vítreo, é recoberto com uma camada de BDD. A camada de BDD pode ser observada por microscopia eletrônica de varredura (SEM), que permite avaliar a morfologia das partículas. Espectroscopia Raman é comumente usada para examinar a microestrutura de BDD, sendo que

materiais de BDD apresentam uma grande variedade de espectros Raman que estão correlacionados com a quantidade de NDC, tamanho de grão e densidade de defeitos. SEM e espectroscopia Raman permitem a distinção de domínios de carbono sp^2 e sp^3, o que permite a correlação da microestrutura dos materiais de BDD com as propriedades eletroquímicas observadas. Essas propriedades podem ser avaliadas por voltametria cíclica, na qual picos redox podem ser observados devido à presença de NDC. Além disso, sistemas redox como $[Fe(CN)_6]^{3-/4-}$ podem ser utilizados, sendo que a sua resposta eletroquímica é sensível a propriedades de superfície ou eletrônicas do BDD. Polarização anódica é usada para analisar a estabilidade dos pós, sendo que pós menos estáveis demonstram maior oxidação. Finalmente, é possível fixar nanopartículas de Pt ao BDD para testar sua viabilidade como possível suporte de eletrocatalisador. Após a fixação das nanopartículas ao BDD, é possível avaliar o desempenho e durabilidade dos potenciais suportes de BDD com as técnicas mencionadas previamente e com testes acelerados de estabilidade a longo prazo.

Palavras-chave: Células a combustível de membrana trocadora de prótons. Diamante dopado com boro. Suporte de eletrocatalisador. Deposição química em fase de vapor. Carbono não diamante. Espectroscopia Raman. Voltametria cíclica.

ABSTRACT

Proton-exchange membrane fuel cells (PEMFCs) are promising candidates for the green conversion of hydrogen into electric energy. A considerable problem preventing the large-scale applications of PEMFCs is the inadequate durability of the supported electrocatalyst layer. Carbon blacks (CBs) such as Vulcan XC-72 are commonly used as the carbon support, however its stability is limiting for long term PEMFC use. CB in the cathode is oxidized in the PEMFC start and stop cycles, detaching the Pt nanoparticles and promoting their agglomeration, which leads to performance loss. This degradation is due to the high potentials caused by fuel starvation and to the accelerated corrosion rate induced by the Pt catalysts. Boron-doped diamond (BDD) has interesting properties, such as high chemical and thermal stability, that make it desirable as a PEMFC electrocatalyst support material. The most widespread method for producing BDD is chemical vapor deposition (CVD), since it is efficient in dopant control and makes diamond with consistent characteristics. The physicochemical and electrical properties of BDD are affected by the amount of non-diamond carbon (NDC) present in the diamond matrix, by the grain size and by the boron doping. All of this in turn are controlled by the CVD conditions that are employed, such as source gas mixture ratios and deposition pressure/power. BDD can be synthesized as a film or a powder; the latter is most wanted for energy applications as it has a higher surface area. BDD particles can be synthesized by a core-shell approach, in which a powder substrate, such as nanodiamond or glassy carbon, is coated with a layer of BDD. The BDD overlayer can be observed with scanning electron microscopy (SEM), which allows the assessment of the particles' morphology. Raman spectroscopy is widely used for evaluation of the BDD microstructure, as BDD materials have a wide range of Raman spectra that correlate with the amount of NDC, grain size and defect density. SEM and Raman spectroscopy enable the distinction of sp^2 and sp^3 bonded carbon domains, which allows the correlation of the BDD mate-

rials' microstructure with the observed electrochemical properties. These properties can be evaluated by cyclic voltammetry, in which redox peaks may be observed due to the presence of NDC. Additionally, redox probes such as $[Fe(CN)_6]^{3-/4-}$ can be used, with the electrochemical response being sensitive to the surface or electronic properties of BDD. Anodic polarization is used to analyze the stability of the powders, as less-stable powders show more extensive oxidation. Finally, it is possible to attach Pt nanoparticles to BDD to test their viability as electrocatalyst support. After attachment of the Pt nanoparticles, it is possible to evaluate the performance and durability of the potential BDD supports with the previously mentioned electrochemical techniques and with accelerated long-term stability tests.

Keywords: Proton-exchange membrane fuel cells. Boron-doped diamond. Electrocatalyst support. Chemical vapor deposition. Non-diamond carbon. Raman spectroscopy. Cyclic Voltammetry.

List of Symbols and Abbreviations

ICE - Internal combustion engine

ICEV - Internal combustion engine vehicle

NO_x - Nitrogen oxides

SO_x - Sulfur oxides

EV- Electric vehicle

BTU – British Thermal Unit

OECD - Organization for Economic Cooperation and Development

AEV - All electric vehicle

HEV- Hybrid electric vehicle

BEV - Battery electric vehicle

PEMFC – Proton-exchange membrane fuel cell

NHE - Normal hydrogen electrode

PFSA - Perfluorosulfonic acid

FCEV- Fuel cell electric vehicle

ORR - Oxygen reduction reaction

COR - Carbon oxidation reaction

MEA - Membrane electrode assembly

BDD - Boron-doped diamond

CVD - Chemical vapor deposition

UNCD - Ultrananocrystalline diamond

NCD - Nanocrystalline diamond

MCD - Microcrystalline diamond

SEM - Scanning electron microscopy

BNCD - Boron-doped nanocrystalline diamond

GC - Glassy carbon

B-UNCD-GC – Boron-doped ultrananocrystalline diamond glassy carbon

NIR - Near infrared

FWHW - Full width at half maximum

NDC - Non-diamond carbon

CV - Cyclic voltammogram

C_{dl} - Background capacitance

ET - Electron transfer

k^{o}_{app} - Heterogeneous electron rate constants

ΔE_p - Peak-to-peak separation

I_{ox}/I_{red} - Oxidation peak current to reduction peak current ratios

Ag/AgCl - Silver/silver chloride reference electrode

SCE - Saturated calomel electrode

RHE – Reversible hydrogen electrode

ECSA - Electrochemically active Pt surface area

MWCNTs - Multi-walled carbon nanotubes

EDX - Energy dispersive X-ray

Table of contents

1) Negative Impacts of Internal Combustion Engine Vehicles

The development and widespread use of internal combustion engine (ICE) vehicles, or ICEVs, is possibly one of humanity's greatest achievements. They have shaped modern society by allowing efficient transportation on a daily basis, being a central part in people's lives and in the global economy. Despite this enormous importance, automobiles and the fossil fuel economy have been leading to vast environmental, social, and economic problems.

Currently, around 99.8% of the global passenger fleet relies on carbon fuels, such as gasoline or diesel (ZARAZUA DE RUBENS; NOEL; KESTER; SOVACOOL, 2020). In most ICEs, hydrocarbons are oxidized to form carbon dioxide, water, and other byproducts, with the release of heat. Greenhouse gases such as CO_2 absorb the Sun's infrared radiation reflected from the ground, leading to an increase in temperature, as is illustrated in Figure 1. This effect is known as global warming and results in major ecological damage, as well as in natural disasters, which affect human populations (EHSANI; GAO; LONGO; EBRAHIMI, 2018). Global warming caused by the burning of fossil fuels has also caused changes in the Earth's climate since the mid-20th century, which are known as climate change (SHAFTEL; JACKSON; SUSAN; DANIEL, 2020).

Besides CO_2, ICEVs emit several other pollutants that result from the combustion of hydrocarbons. Nitrogen and sulfur impurities present in hydrocarbons react with oxygen from the air to form nitrogen oxides (NO_x) and sulfur oxides (SO_x). These oxides react with water to form H_2SO_4 and HNO_3, leading to acid rain, which is harmful to fish, vegetation and other biota (BURNS; AHERNE; GAY; LEHMANN, 2016). Additionally, ICEs lead to some incomplete combustion of hydrocarbons, resulting in the formation of carbon monoxide and the presence of unburned hydrocarbons, which in turn have adverse effects on human health and the environment (SCHNEIDER, 2002).

Figure 1 - Natural occurring greenhouse effect (on the left) versus human induced global warming (on the right). Source: ref. ("What is Climate Change?", 2019).

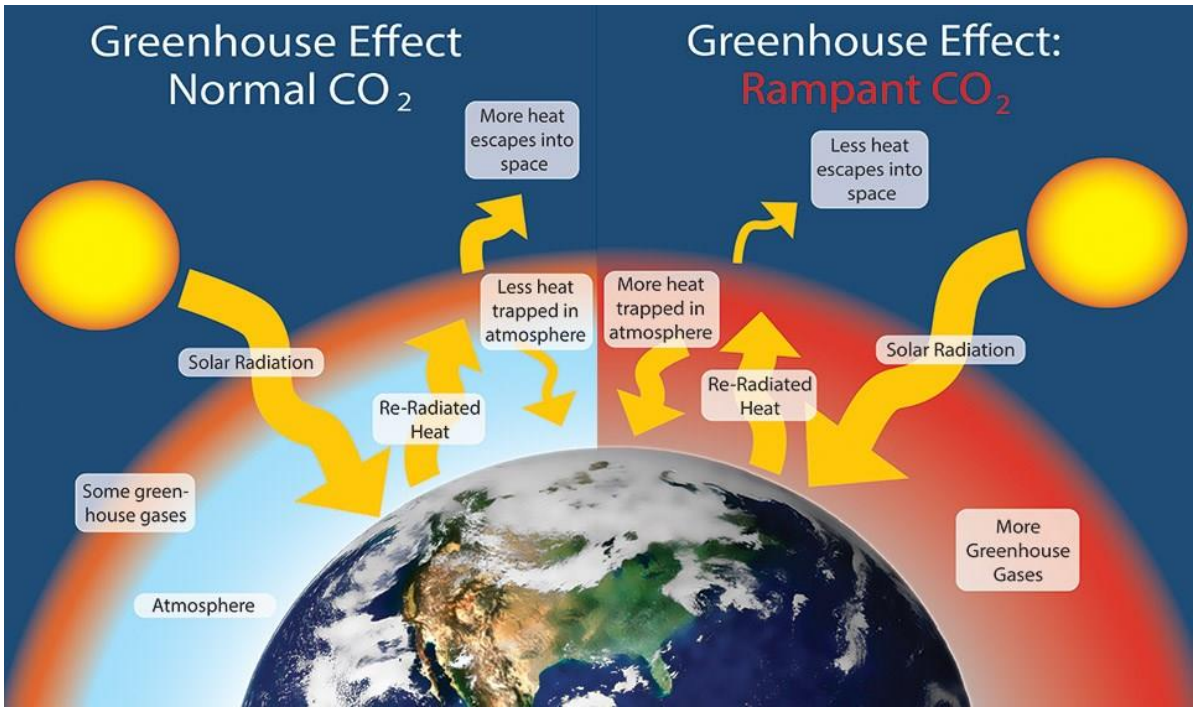

Every year of rising emissions endangers and threatens economies and the livelihoods of billions of people (FIGUERES; LE QUERE; MAHINDRA; BATE; WHITEMAN; PETERS; GUAN, 2018). In 2017, for example, disasters triggered by weather and climate amounted to US$320 billion in damages and cost about 10,000 lives (LÖW, 2018). In the past two decades, natural disasters such as wildfires and typhoons likely contributed to an exponential rise in damages, amounting to around US$2.2 trillion ("UN 20-year review: earthquakes and tsunamis kill more people while climate change is driving up economic losses", 2018). Besides these profound costs, global warming has also likely increased income inequality (DIFFENBAUGH; BURKE, 2019). This is due to the connection found between temperature and economic growth, with warming increasing growth in cool countries and decreasing growth in warm countries. There is also a connection between climate change and human conflicts; potential changes in temperature and precipitation in the upcoming decades could lead to aggravated

rates of human conflicts and lead to a large social impact (HSIANG; BURKE; MIGUEL, 2013).

Warmer temperatures lead to more frequent and prolonged heat waves, which consequently lead to more heat wave related deaths and adverse effects on society's mental and physical health (DODGEN; DONATO; KELLY; LA GRECA; MORGANSTEIN; RESER; RUZEK; SCHWEITZER; SHIMAMOTO; THIGPEN TART; URSANO, 2016). People with mental illness are particularly vulnerable to extreme heat or heat waves. In a study involving 1065 heat wave-related deaths, it was observed that preexisting mental illness tripled the risk of death due to heat wave exposure (BOUCHAMA; DEHBI; MOHAMED; MATTHIES; SHOUKRI; MENNE, 2007). Heat waves are also associated with mood disorders, anxiety, psychological and physical fatigue, heat-related violence, and lower average birth rate (CIANCONI; BETRÒ; JANIRI, 2020). The homeless are especially vulnerable to heat waves and climate change in general, as they suffer from high rates of chronic diseases, mental illnesses, respiratory conditions and live in urban areas, which are prone to the urban heat island effect (RAMIN; SVOBODA, 2009).

Higher temperatures and climate change can worsen air quality, leading to respiratory health effects and cardiovascular effects (FANN; BRENNAN; DOLWICK; GAMBLE; ILACQUA; KOLB; NOLTE; SPERO; ZISKA, 2016). An increase in temperature leads to an increase in surface ozone,(BLOOMER; STEHR; PIETY; SALAWITCH; DICKERSON, 2009) which can lead to irritation of the respiratory system, damage of lung function and reduction of agricultural yields (ZHONG; LEE; HAGHIGHAT, 2017). Particulate matter is another pervasive air quality problem linked to climate change; when inhaled, particulate matter can lead to significant health problems, such as asthma, chronic bronchitis, reduced lung function, heart attack and premature death (DAWSON; BLOOMER; WINNER; WEAVER, 2013).

As can be seen in Figure 2, the Earth will reach a warming level of 1.5 °C by 2036 and of 2 °C by 2063 with the current rate of progression. In 2015, 196 nations agreed to limit global warming to well below 2 °C, and to strive for 1.5 °C by adopting the Paris climate agreement. To achieve this goal and minimize damages, substantial changes must occur in the world's energy matrix, transportation systems, and industries. Global CO_2 emissions must start to fall by 2020 so that that temperature goal can be achieved (FIGUERES; SCHELLNHUBER; WHITEMAN; ROCKSTRÖM; HOBLEY; RAHMSTORF, 2017). Additionally, mankind must achieve net zero CO_2 emissions by 2050, even with a temporary overshoot of 2 °C in temperature increase (MASSON-DELMOTTE; ZHAI; PÖRTNER; ROBERTS; SKEA; SHUKLA; PIRANI; MOUFOUMA-OKIA; PÉAN; PIDCOCK; CONNORS; MATTHEWS; CHEN; ZHOU; GOMIS; LONNOY; MAYCOCK; TIGNOR; WATERFIELD, 2018).

Figure 2 - Global temperature anomalies. Source: ref. (RHODE, 2020).

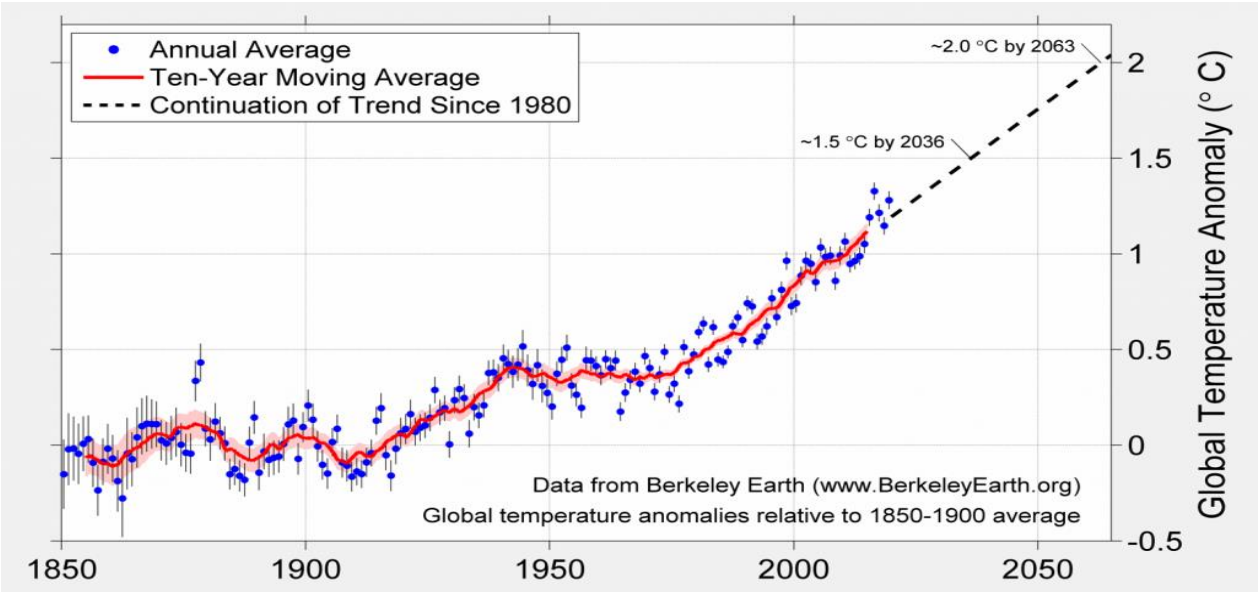

Regarding the global temperature increase, every fraction of a degree can have profound social, environmental, and economic effects. By the end of the 21st century, there is a high chance that limiting the temperature to 1.5 °C would

reduce economic damages relative to 2 °C; these benefits could exceed US$20 trillion and also lessen global inequality (BURKE; DAVIS; DIFFENBAUGH, 2018). It is therefore of profound importance that global warming be limited, which inevitably involves the transition from fossil fuels to clean energy sources. This means undoubtedly that ICEVs are becoming more and more a technology of the past, as cleaner alternatives emerge and develop.

2) Electric Vehicles and Fuel Cells: Alternatives to Fossil Fuels

One of humanity's greatest challenges is to find suitable and clean replacements for fossil fuels, since their use is unsustainable and the world energy consumption is growing, as can be seen in Figure 3. Alternatives are being intensely sought and must be economically feasible, efficient, and environmentally friendly. In the next four decades, renewable energy could account for 80% of the world's energy supply, (ALASWAD; DASSISTI; PRESCOTT; OLABI, 2015) as the world is moving towards a clean, cheap, and reliable energy system (FIGUERES; LE QUERE; MAHINDRA; BATE; WHITEMAN; PETERS; GUAN, 2018). Electric vehicles (EVs) are seen as a solution to decarbonize passenger transportation in the world, (MUNEER; MILLIGAN; SMITH; DOYLE; POZUELO; KNEZ, 2015) and are being incentivized by policies that encourage their purchase (LANGBROEK; FRANKLIN; SUSILO, 2016).

Figure 3 - World energy consumption, with the contributions of OECD and non-OECD countries. Source: ref. (“International Energy Outlook 2019”, 2019).

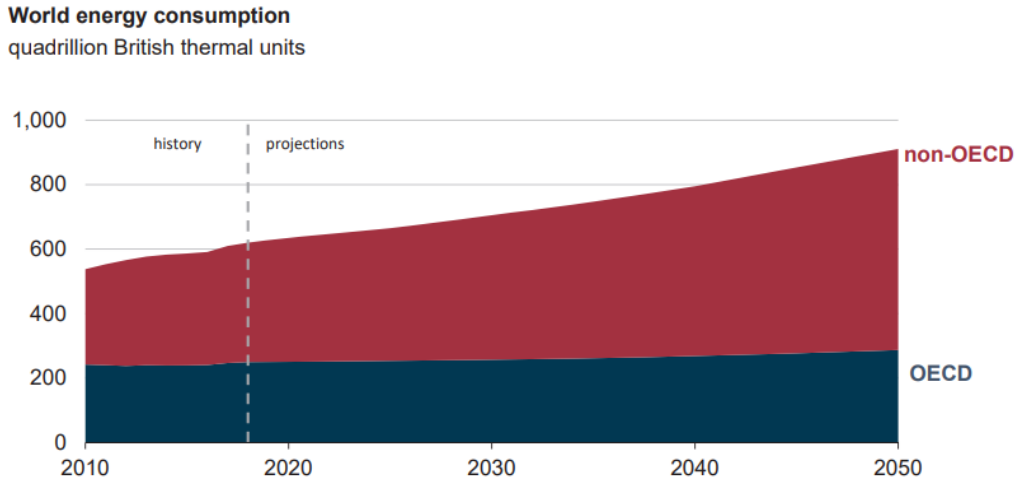

Briefly, ICEVs have a combustion chamber that converts chemical energy from a fuel, such as gasoline, to thermal energy, which is then converted to kinetic energy. All-electric vehicles (AEVs) use only electric power as the source of energy, while a hybrid electric vehicle (HEV) is a vehicle that uses both an ICE and an electric motor as energy sources. As can be seen in Figure 4, the energy source of AEVs can be either a battery or a fuel cell. A fuel cell is an electrochemical device that converts chemical energy of a fuel into electricity and heat with high efficiency (SPIEGEL, 2007). The difference between a fuel cell and a battery is that the reactants of a fuel cell are being continuously fed into the cell, while in a battery the reactants are stored and consumed (WILBERFORCE; ALASWAD; PALUMBO; DASSISTI; OLABI, 2016).

Figure 4 - Classification of vehicles according to their energy source. Source: ref. (DAS; TAN; YATIM, 2017).

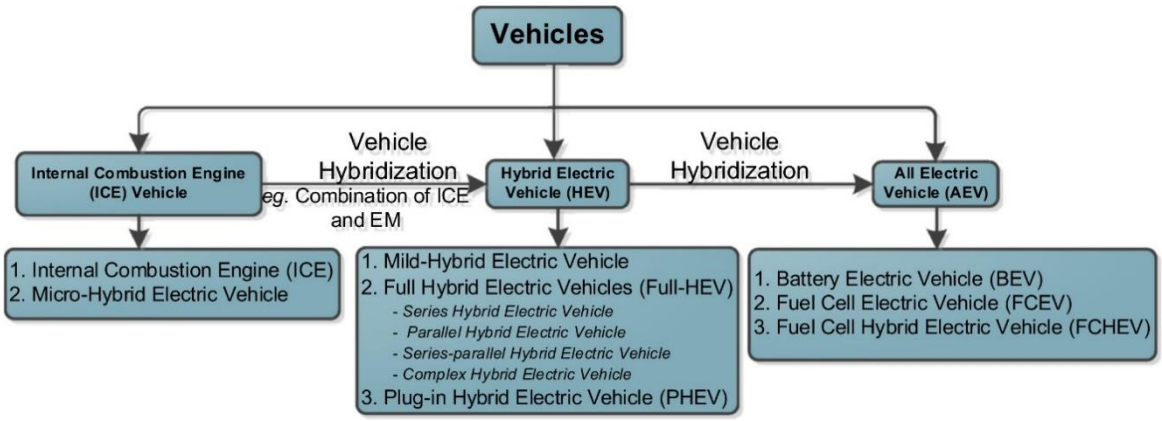

Historically, the adoption of EVs has been faced with challenges and continues to present many barriers. The first mass produced EV of the modern era was the General Motors EV1, produced and leased by General Motors in the period 1996-1999. This car was a battery electric vehicle (BEV) that failed to compete in the market. EV1 drivers coined the term range anxiety, which makes explicit their constant fear of becoming stranded with a discharged battery away from electric infrastructure (WILBERFORCE; EL-HASSAN; KHATIB; AL; BAROUTAJI; CARTON; OLABI, 2017), a challenge up to this day. Another reason for the slow adherence to EVs is the high cost of batteries (NEWBERY; STRBAC, 2016). The problems of EV adoption can be summarized as issues with driving, capacity, taxation, policy incentives, and charging infrastructure. Additionally, battery and fuel cell systems must face the increasing sales of cheaper ICEVs in emerging countries (DIJK; ORSATO; KEMP, 2013).

Hydrogen is believed by many to be the fuel of the future, but it is not considered a primary energy source like fossil fuels. Hydrogen is not found as H_2 in the Earth, so it has to be produced from compounds that contain hydrogen atoms. However, it is an interesting energy carrier because its combustion produces only energy and water as the reaction products (CIPRIANI; DI DIO;

GENDUSO; LA CASCIA; LIGA; MICELI; RICCO GALLUZZO, 2014). Other advantages of hydrogen are (SPIEGEL, 2007): it can be made from various sources and is completely renewable, it can be stored in many forms and physical states, it can be converted to, and produced from, electricity with high efficiency, and it can be transported as safely as other fuels. Despite the great potential of hydrogen as a fuel, a hydrogen-based economy still involves daunting technical and economic difficulties (STEELE; HEINZEL, 2001). Major challenges are the H_2 price at the pump, hydrogen infrastructure and storage, durability of fuel cells, and clean H_2 production methods (CIPRIANI; DI DIO; GENDUSO; LA CASCIA; LIGA; MICELI; RICCO GALLUZZO, 2014; LE; SMATTI, 2014; STEELE; HEINZEL, 2001; WILBERFORCE; EL-HASSAN; KHATIB; AL; BAROUTAJI; CARTON; OLABI, 2017).

A fuel cell is made of an electrolyte layer sandwiched between two porous electrodes, with one being negatively charged (anode) and the other being positively charged (cathode). Both electrodes contain catalysts to accelerate the chemical reactions. The classification of fuel cells is done primarily by the type of electrolyte that they use (which determines the electrochemical reactions that take place), the fuel, the temperature range, and the type of catalysts that are employed (“Types of Fuel Cells”, 2020).

The polymer electrolyte (or proton-exchange) membrane fuel cell (PEMFC) is considered one of the most promising future energy-conversion devices, due to its fast startup, high efficiency, low operation temperature, high power density, system robustness, flexibility of fuel type, and reduced sealing, corrosion, shielding or leakage concerns (WANG; JIANG, 2017; WILBERFORCE; EL-HASSAN; KHATIB; AL; BAROUTAJI; CARTON; OLABI, 2017). It contains a polymer membrane that is impermeable to gases but conducts protons and acts as the electrolyte (BARBIR, 2006). In a PEMFC, hydrogen is oxidized at the anode and oxygen is reduced at the cathode. When hydrogen is oxidized at the anode, it releases protons and electrons, as can be seen

in Figure 5. The polymer electrolyte then conducts protons from the anode to the cathode, while electrons flow through the external circuit. At the cathode, electrons combine with oxygen to form water and heat. The reactions involved in a PEMFC are represented by the following equations:

Anode: $H_2 \rightarrow 2H^+ + 2e^-$ E° = 0.0 V vs. NHE (1)

Cathode: $½O_2 + 2H^+ + 2e^- \rightarrow H_2O$ E° = 1.229 V vs. NHE (2)

Overall: $H_2 + ½O_2 \rightarrow H_2O$ E° = 1.229 V vs. NHE (3)

Figure 5 - Diagram of a PEMFC. Source: ref. (MATTUCI, 2020).

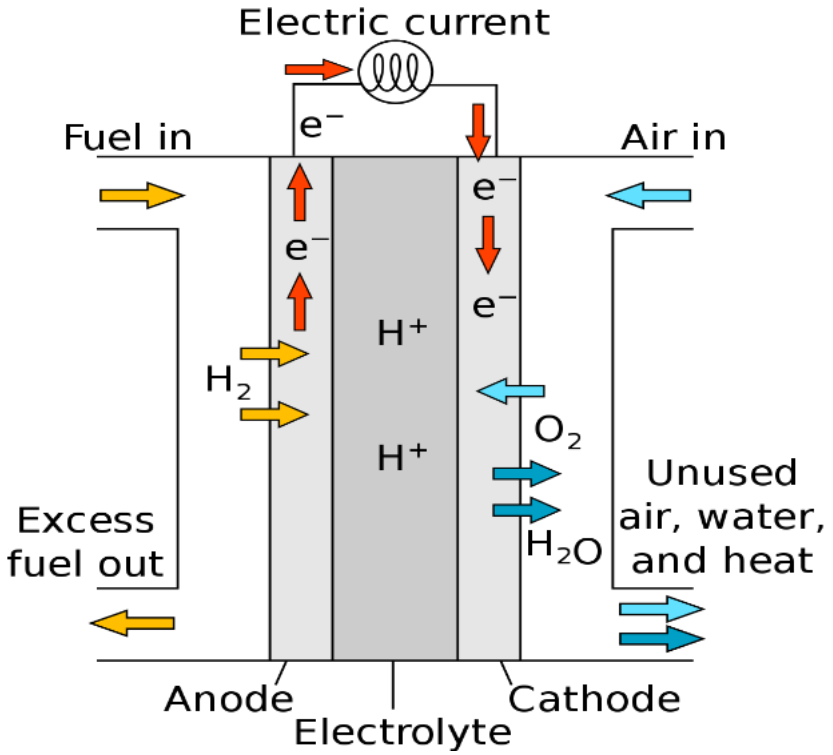

The polymeric electrolyte must be a charge carrier for protons, an electronic insulator so electrons do not pass through the membrane and, additionally, must separate reactant gases (PEIGHAMBARDOUST; ROWSHANZAMIR; AMJADI, 2010). The standard electrolyte material currently being used for PEMFCs is a fluorinated teflon-based material made by DuPont with the generic name of Nafion (WILBERFORCE; EL-HASSAN; KHATIB; AL; BAROUTAJI;

CARTON; OLABI, 2017). PEMFCs that use membranes based on perfluorosulfonic acid (PFSA) such as Nafion have a fast startup, high efficiency, low operation temperature (80 °C or lower), high power density, easy assembly and handling, and are the most developed technologies for the expansion of FCEVs (WANG; JIANG, 2017).

A fuel cell electrode is a thin catalyst layer situated between the membrane and a porous, electrically conductive substrate, in which the electrochemical reactions take place (see Figure 6). The electrocatalyst must meet several performance, durability, and cost targets, such as endurance of tens of thousands of start-up/shut-down events (DEBE, 2012). Currently, Pt-based nanoparticles are the most common catalysts and the only electrocatalysts presently used in applied PEMFCs (MAJLAN; ROHENDI; DAUD; HUSAINI; HAQUE, 2018; WANG; ZHAO; FANG; LI; BI; WANG, 2015). Out of all pure metals, platinum supported on carbon has the highest catalytic activity for the oxygen reduction reaction (ORR) (WANG; ZHAO; FANG; LI; BI; WANG, 2015) and presents a high chemical stability, exchange current density, and work function (SHARMA; POLLET, 2012). Both the anode hydrogen oxidation reaction and the cathode ORR occur on the surfaces of Pt-based catalysts (DEBE, 2012). The H_2 oxidation reaction is kinetically rapid at the Pt anode while the kinetics of the ORR is very sluggish, even with Pt catalysts, which results in a major voltage loss at the Pt cathode (FANG; KIM; LEE; YU, 2008). Additionally, platinum is very expensive, with the catalyst accounting for 55% of the PEMFC cost (TASIC; MILJANIC; MARCETA KANINSKI; SAPONJIC; NIKOLIC, 2009). Despite the high cost of Pt and its limited reserves, Pt electrocatalysts can be recycled and thus are considered the main players in PEMFCs for the near future (WANG; JIANG, 2017).

Figure 6 - Diagram of a membrane electrode assembly. Source: ref. (BARBIR, 2006).

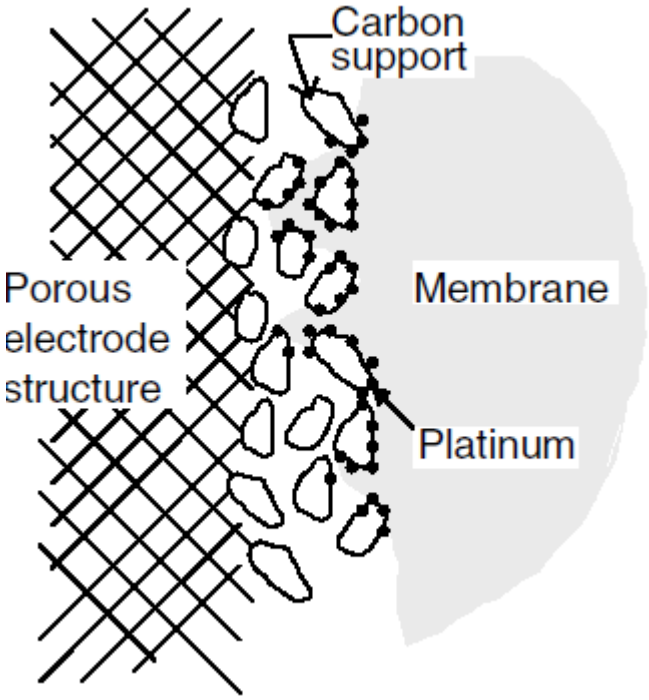

Catalyst layers must be relatively thin to minimize losses due to the rate of proton diffusion within the catalyst layer and the rate of mass transfer of reactants and products to and from the active sites (DICKS, 2006). Consequently, supporting materials are necessary to distribute and stabilize the catalyst particles (FANG; KIM; LEE; YU, 2008). These highly dispersed electrocatalyst particles on a stable and conductive support increase the number of electrochemical active sites available for reaction in the fuel cell (AY, 2011). Therefore, the catalyst support plays a very important role in PEMFCs. Ideally, they should have (SHARMA; POLLET, 2012):

i) High electrical conductivity;
ii) Favorable catalyst-support interaction;
iii) Large surface area;
iv) Water handling capability to avoid flooding;

v) High corrosion resistance;

vi) Easy recovery of the catalyst.

Commonly, carbon supports are used as they fulfill most of these requirements, providing a relatively large surface area and adequate electrical conductivity (STEVENS; DAHN, 2005). Compared with other catalyst supports, such as alumina and MgO, carbon is generally stable in either acidic or basic media, and additionally can be burned off to recover the platinum (DICKS, 2006). A variety of carbon materials are being studied, such as graphitic carbons. These carbons may have higher corrosion resistance than disordered carbons; however, they present low surface areas, which leads to problems (CHUNG; HAM; KANG; JU; LEE, 2020). For this reason, high surface area carbons, i.e. carbon blacks such as Vulcan XC72R, are used (RALPH; HOGARTH, 2002).

Despite their widespread use, durability issues with these carbon materials remain a barrier for adequate PEMFC lifetime targets to be met. Corrosion of the carbon support will lead to loss of the electrocatalyst, drastically affecting the overall performance of the fuel cell (SHARMA; POLLET, 2012). As illustrated in Figure 7, this corrosion of the carbon support will weaken the interaction between the support and the platinum nanoparticles, causing their detachment, agglomeration, and dissolution, with the consequent reduction of electrochemical area (DU; SHAO; SUN; YIN; LIU; WANG, 2016; ZHANG; YANG; GUO; LIU, 2016).

Figure 7 - Illustration of the degradation of Pt electrocatalyst in a PEMFC MEA. Source: ref. (DU; SHAO; SUN; YIN; LIU; WANG, 2016).

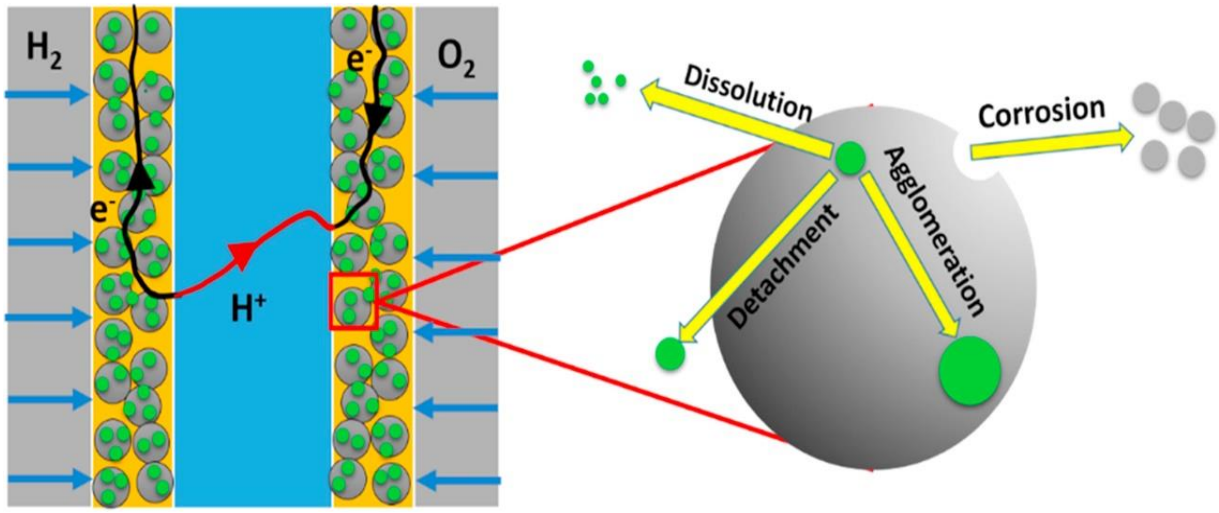

The electrochemical corrosion of carbon occurs through the following reaction:

$$C + 2H_2O \rightarrow CO_2 + 4H^+ + 4\,e^- \qquad E° = 0.207\ V\ vs.\ NHE \qquad (4)$$

This carbon oxidation reaction (COR) is thermodynamically possible in normal PEMFC conditions; however, its rate is only significant at potentials higher than 1.0-1.1 V versus NHE (CASTANHEIRA; SILVA; LIMA; CRISCI; DUBAU; SA, 2015). During start/stop events or fuel starvation events, these elevated potentials are reached and cause significant carbon corrosion (CASTANHEIRA; DUBAU; MERMOUX; BERTHOME; CAQUE; ROSSINOT; CHATENET, 2014). Additionally, the corrosion rate of the carbon support is accelerated by Pt-based catalysts (ROEN; PAIK; JARVI, 2004).

During fuel starvation, that is, when the amount of fuel is insufficient to provide the expected current for the PEMFC, the anode potential is increased and can be even higher than the cathode potential. In this condition, carbon can be consumed, as described by equation 4, to provide electrons for the ORR at the cathode. Fuel starvation can happen in the startup and shut down of the PEMFC,

in which uneven distribution of gas may occur, leading to the consumption of the carbon support (ZHANG; WANG; CHEN; PEI, 2018).

Due to the carbon support degradation, which deeply affects PEMFC performance and durability, a wide range of different materials is being investigated. These include carbon nanotubes, carbon nanofiber, graphene, mesoporous carbon, BDD, and even non-carbonaceous compounds (DU; SHAO; SUN; YIN; LIU; WANG, 2016; SHARMA; POLLET, 2012). BDD has some very interesting properties that make it highly desired as an electrocatalyst support material. These properties include high chemical and thermal stability, extreme hardness, a high corrosion resistance and a low background current (SALAZAR-BANDA; EGUILUZ; AVACA, 2007; SWAIN, 1994).

3) Boron-Doped Diamond: Synthesis and Properties

Diamond is a very well-known allotrope of carbon. It is made of sp^3 hybridized carbon atoms arranged tetrahedrally, with each carbon atom making four covalent bonds with four other carbon atoms. These atoms are arranged in six membered rings, with each ring in a “chair” conformation. This molecular bonding and structure leads to extreme properties, such as hardness, very high thermal conductivity and electric resistivity; diamond has a very wide-band gap of 5.47 eV at 300 K (BARTLETT; ALKIRE; LIPKOWSKI, 2015).

However, just like silicon, diamond can be doped to alter its electrical properties, i.e. it can become an electrically conductive material. Diamond can be doped with boron, whose atoms form a band located ~0.35 eV above the valence band edge (XU; GRANGER; CHEN; STROJEK; LISTER; SWAIN, 1997). Vacancies in the valence band form because at room temperature some of the valence bands electrons are thermally promoted to the boron acceptors, allowing the flow of electrical current. Nitrogen can also be used as a dopant, but it has a higher activation energy of 1.7 eV. Boron’s lower activation energy allows high doping

levels, consequently making this element the preferred dopant for electrochemical studies (MACPHERSON, 2015).

As previously mentioned, the most widespread method for growing BDD is by chemical vapor deposition (CVD) because it yields diamond available with consistent characteristics, tailored to specific applications, and is efficient in the control of dopant incorporation (BALMER; BRANDON; CLEWES; DHILLON; DODSON; FRIEL; INGLIS; MADGWICK; MARKHAM; MOLLART; PERKINS; SCARSBROOK; TWITCHEN; WHITEHEAD; WILMAN; WOOLLARD, 2009; ZANIN; MAY; FERMIN; PLANA; VIEIRA; MILNE; CORAT, 2014). In the synthesis conditions of the CVD reactor, diamond is metastable compared to graphite. The synthesis of diamond by CVD is driven by kinetics and not thermodynamics (BALMER; BRANDON; CLEWES; DHILLON; DODSON; FRIEL; INGLIS; MADGWICK; MARKHAM; MOLLART; PERKINS; SCARSBROOK; TWITCHEN; WHITEHEAD; WILMAN; WOOLLARD, 2009). This synthesis, which depends on the generation of carbon radicals and dissociated hydrogen, can be thought of as an addition of these carbon atoms to the existing diamond lattice, as illustrated in Figure 8.

Figure 8 - Diagram of simplified reaction scheme occurring at the diamond surface. Source: ref. (AY, 2011).

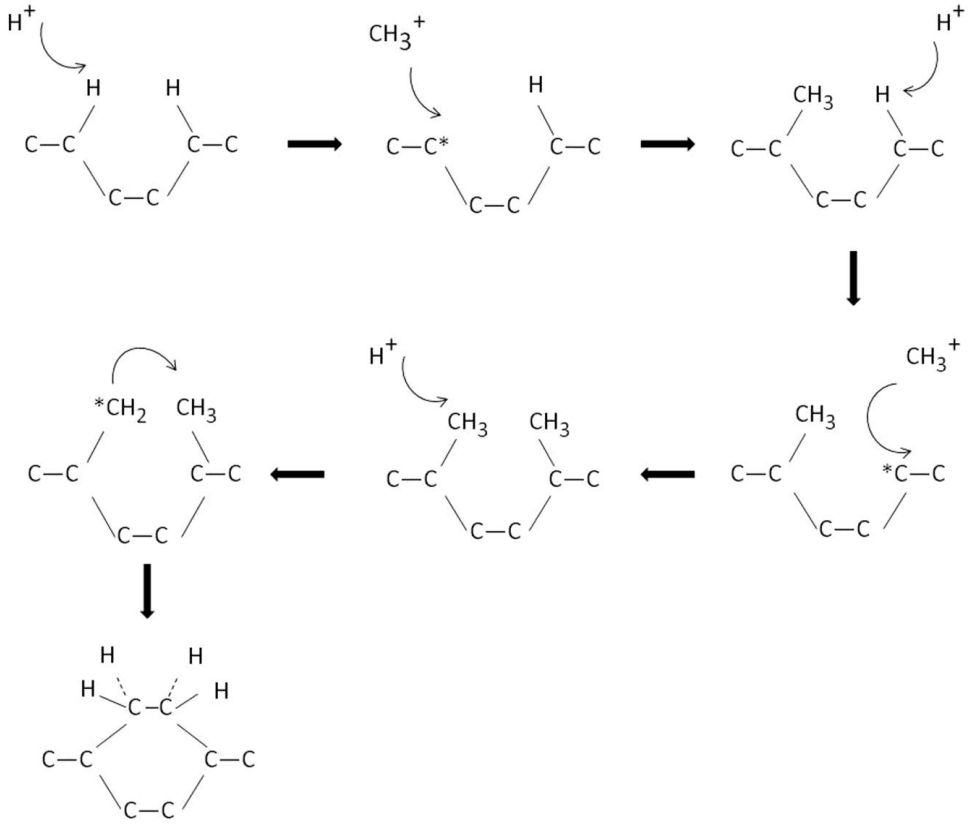

In the CVD technique, a plasma is created by a microwave or hot filament. A source gas mixture containing hydrogen, a boron compound (such as diborane), and carbon source (usually methane) is introduced into the plasma to be thermally activated. Carbon radicals are formed and BDD is then deposited into the substrate. Typical CVD conditions are C/H volume ratios of 0.5-2%, pressures of 10-100 Torr, substrate temperatures of 800-1000 °C and microwave power of 1000-1300 W or filament temperatures of 2100 °C, depending on the selected method (XU; GRANGER; CHEN; STROJEK; LISTER; SWAIN, 1997). The CVD growth of a BDD overlayer on seed diamond based on a microwave assisted plasma is illustrated in Figure 9, in which the conditions are also informed.

Figure 9 - Illustration of CVD growth of BDD on a seed diamond. Source: ref. (AY; SWOPE; SWAIN, 2008).

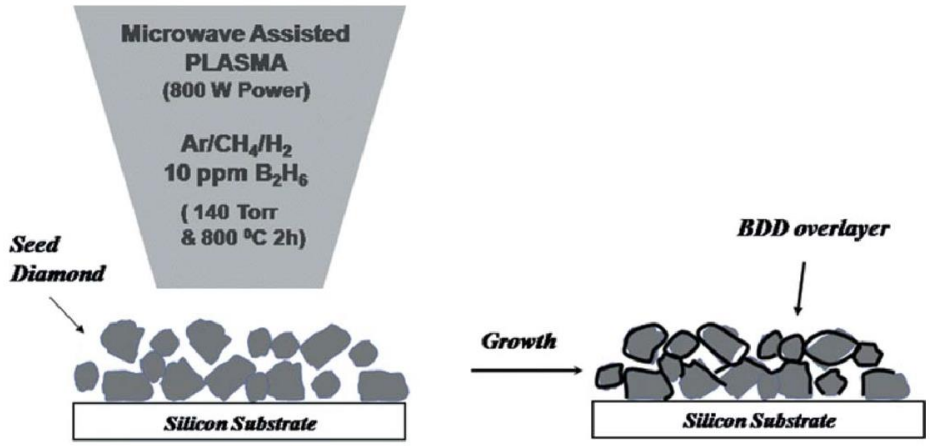

Hydrogen atoms perform many important functions in the synthesis of BDD by CVD. They etch surface graphitic (sp^2-bonded) carbon several times faster than any diamond-like (sp^3-bonded) carbon (MAY; HARVEY; SMITH; MANKELEVICH, 2006). Additionally, H atoms help terminate "dangling" bonds on the diamond surface, helping its stabilization during growth. They also prevent polymer buildup and create radical sites on the surface by abstraction of surface hydrogen atoms, removing some terminal hydrogen atoms from the substrate.

Macroscopic solids can be generally divided in three classes: amorphous, polycrystalline, and single crystal (BALMER; BRANDON; CLEWES; DHILLON; DODSON; FRIEL; INGLIS; MADGWICK; MARKHAM; MOLLART; PERKINS; SCARSBROOK; TWITCHEN; WHITEHEAD; WILMAN; WOOLLARD, 2009). BDD made by CVD can be classified as either polycrystalline or single crystal. When the substrate in the CVD reactor is bulk diamond (natural of artificial), single crystal BDD is obtained. However, when a non-diamond substrate is used, then polycrystalline BDD is obtained (YANG; YU; MACPHERSON; EINAGA; ZHAO; ZHAO; SWAIN; JIANG, 2019). Poly-

crystalline diamond is made of crystallites with different orientations and associated grain boundaries, while single crystal diamond has no grain boundaries, as can be seen in Figure 10.

Figure 10 - Illustration of single crystal, polycrystalline and amorphous solids. Source: ref. ("Illustration of single crystal, polycrystalline and amorphous solids", [s.d.]).

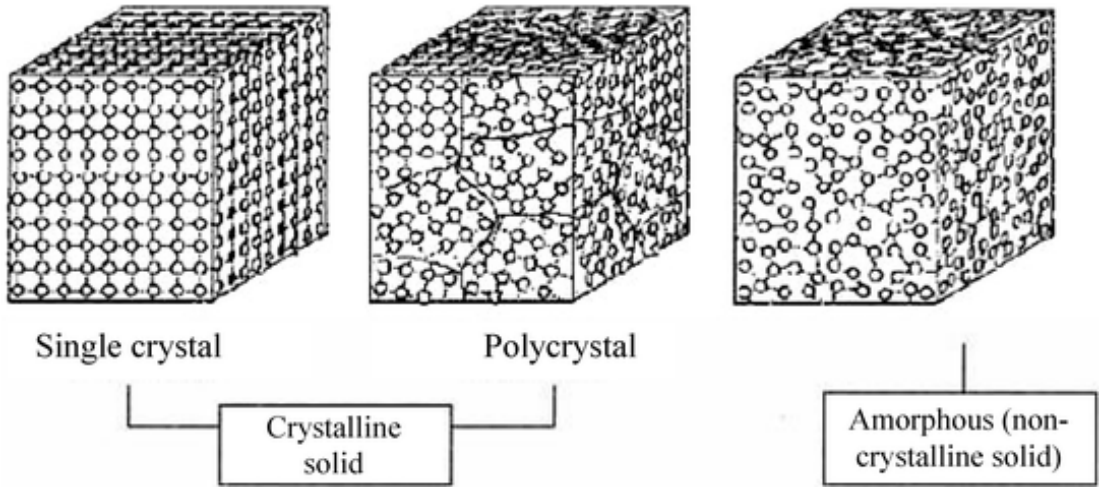

Diamond does not grow spontaneously on non-diamond materials, therefore a seeding step is necessary for deposition on a non-diamond substrate, such as silicon (YANG; YU; MACPHERSON; EINAGA; ZHAO; ZHAO; SWAIN; JIANG, 2019). Diamond nanoparticles can be used as initial nucleation sites for growth; the diamond grains then coalesce, forming a continuous polycrystalline diamond film. Polycrystalline BDD films are classified according to their crystallite or grain size, which can vary from being < 10 nm for ultrananocrystalline diamond (UNCD), < 1 μm for nanocrystalline diamond (NCD) ,and > 1 μm for microcrystalline diamond (MCD) (BARTLETT; ALKIRE; LIPKOWSKI, 2015). SEM micrographs of these different polycrystalline BDD films can be seen in Figure 11.

Figure 11 - Scanning Electron Microscopy (SEM) images of the different possible polycrystalline BDD films. Sources: (A) and (B), ref. (WANG; SWOPE; BUTLER; FEYGELSON; SWAIN, 2009); (C) ref. (MAY; LUDLOW; HANNAWAY; HEARD; SMITH; ROSSER, 2008).

(A) Ultrananocrystalline film. **(B)** Nanocrystalline film.

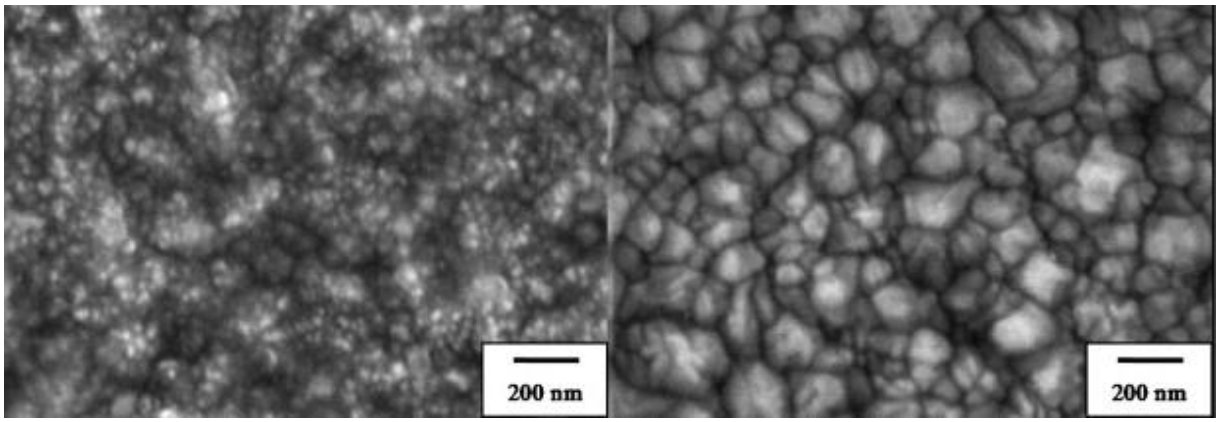

(C) Microcrystalline film.

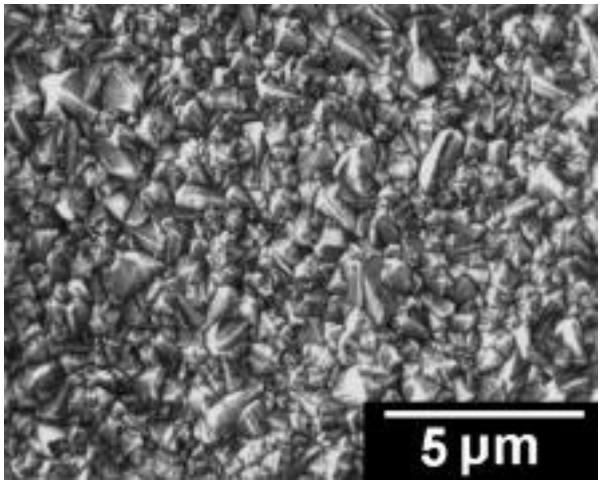

The grain size can be affected by the film thickness; increasing film thickness leads to increasing grain size, (ZAPOL; STERNBERG; CURTISS; FRAUENHEIM; GRUEN, 2002) as can be seen in Figure 12. This heterogeneity in BDD films can be observed not only regarding grain size, but also with boron uptake. Different grains may possess different boron concentrations, which lead to them having different electrical and electrochemical properties (WILSON;

CLEWES; NEWTON; UNWIN; MACPHERSON, 2006). Furthermore, the grain size can also be controlled by changing the seeding method, growth conditions, gas composition, temperature, and pressure (BARTLETT; ALKIRE; LIPKOWSKI, 2015). For example, with proper substrate preparation and seeding, a high nucleation density can be obtained, leading to smaller crystallites (WANG; SWOPE; BUTLER; FEYGELSON; SWAIN, 2009).

Figure 12 - Schematic of the side on growth of boron-doped MCD, showing how grain size increases with film thickness. Source: ref. (MACPHERSON, 2015).

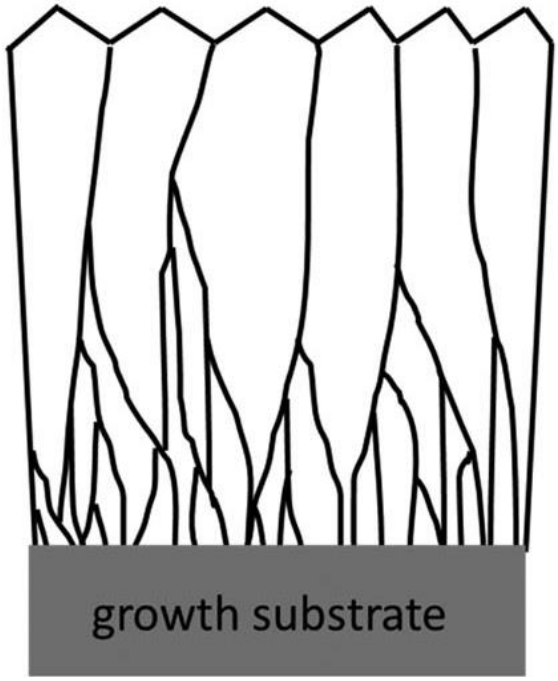

A high nucleation density, leading to smaller crystallites, can also be obtained with the use of argon-rich gas mixtures. When there is a high amount of argon in the source gas mixture, collisions between carbon radicals and argon do not result in any reactions, making it possible for these reactive species to exist long enough and contribute to diamond growth (AY, 2011). The growth from both CH_3 and CH_x drives the surface to continually renucleate or restructure during growth, leading to the formation of very small grain sizes.

Another way to increase the renucleation rate, leading to smaller grain size, is to increase the ratio of methane in the standard CH_4/H_2 gas mixture. When the CH_4/H_2 ratio is increased from 1% to ~5%, the grain size decreases, leading to the formation of NCD films (MAY; HARVEY; SMITH; MANKELEVICH, 2006), which are smoother than the MCD films but still possess a faceted morphology. The grain size determines the surface to volume ratio, which is the determining factor in sp^2 and hydrogen content (WILLIAMS, 2011). Smaller grains lead to higher surface areas and higher sp^2 content, which is thought to occur mostly at grain boundaries. These π-bonded grain boundaries have a deep effect on the mechanical, electrical, and optical properties of the BDD films (SHOW; WITEK; SONTHALIA; SWAIN, 2003). UNCD, usually produced by an Ar-rich source gas mixture, has therefore a significant amount of sp^2 impurities due to its small grain size and large number of grain boundaries. The π-bonded grain boundaries lead to some intrinsic electrical conductivity, that is, conductivity without boron doping (YANG; YU; MACPHERSON; EINAGA; ZHAO; ZHAO; SWAIN; JIANG, 2019). Additionally, the sp^2 content is affected not only by the grain size of the diamond, but also by the reactor conditions employed, such as: (i) substrate temperature; (ii) methane (CH_4) concentration; (iii) deposition pressure; (iv) microwave power, and (v) atomic hydrogen (AYRES; NEWLAND; NEWTON; MANDAL; WILLIAMS; MACPHERSON, 2017). UNCD can also be produced with a H-rich/Ar-lean gas composition and a CH_4/H_2 ratio significantly higher than conventionally used, so the renucleation rate is increased (ZENG; KONICEK; MOLDOVAN; MANGOLINI; JACOBS; WYLIE; ARUMUGAM; SIDDIQUI; CARPICK; CARLISLE, 2015). Regarding its surface, it possesses a nodular morphology with minimal crystal faceting (WANG; SWOPE; BUTLER; FEYGELSON; SWAIN, 2009).

The surface of BDD has external termination bonds, which define physical and chemical properties, being therefore an important factor in possible

applications. The surface of hydrogen-terminated BDD is non-polar, hydrophobic, highly conductive, and possesses a low charge-transfer resistance (RYL; BURCZYK; BOGDANOWICZ; SOBASZEK, 2016). However, the surface of BDD becomes hydrophilic, polar, and poorly conductive when it is oxygen terminated. One way to convert a hydrogen-terminated surface to an oxygen-terminated surface is by anodic polarization, which consists in applying a positive potential to the BDD film (SIMON; GIRARD; BALLUTAUD; GHODBANE; DENEUVILLE; HERLEM; ETCHEBERRY, 2005).

BDD can be synthesized not only as a film, but also as a powder. Since PEMFCs electrocatalyst support materials need to possess a relatively high surface area to evenly distribute the Pt nanoparticles, powder materials are more desirable as they have higher surface areas than films. One way to produce BDD powder is by first depositing a BDD film on silicon by CVD, then dissolving the Si substrate and finally crushing the BDD film until it is a thin powder (SALAZAR-BANDA; EGUILUZ; AVACA, 2007). Additionally, BDD can be produced in powder form by a core shell approach, which consists of coating a powder substrate, such as nanodiamond or a sp^2 carbon powder, with a layer of BDD. The specific surface area of the resulting BDD powder can vary from a few $m^2\ g^{-1}$ to > 100 $m^2\ g^{-1}$ by simply changing the diameter of the substrate powder (YANG; YU; MACPHERSON; EINAGA; ZHAO; ZHAO; SWAIN; JIANG, 2019).

Ay et al. (AY; SWOPE; SWAIN, 2008) reported the preparation of electrically conducting diamond powders by coating 500 nm and 100 nm diamond particles with boron-doped NCD (BNCD) – see Figure 13. An Ar-rich source gas mixture of 1% CH_4, 5% H_2, 94% Ar, and 10 ppm of B_2H_6 was used to coat the surface of these diamond particles by CVD, with a deposition time of 2 h. Later on the Swain group (KIM; MERZOUGUI; SWAIN, 2009) reported the preparation of glassy carbon (GC) powder coated with a layer of boron-doped UNCD (B-UNCD), using a gas mixture of 1% CH_4, 7% H_2, 92% Ar, and 10 ppm of B_2H_6 –

see Figure 14. The 500 nm and 100 nm BNCD coated particles have specific surface areas of 8 and 27 $m^2 g^{-1}$, respectively.

Figure 13 - Scanning Electron Microscopy (SEM) images of 500 nm and 100 nm diamond powder **(A)** and **(C)** before, and **(B)** and **(D)** after deposition of boron-doped NCD for 2 h. Source: ref. (AY; SWOPE; SWAIN, 2008).

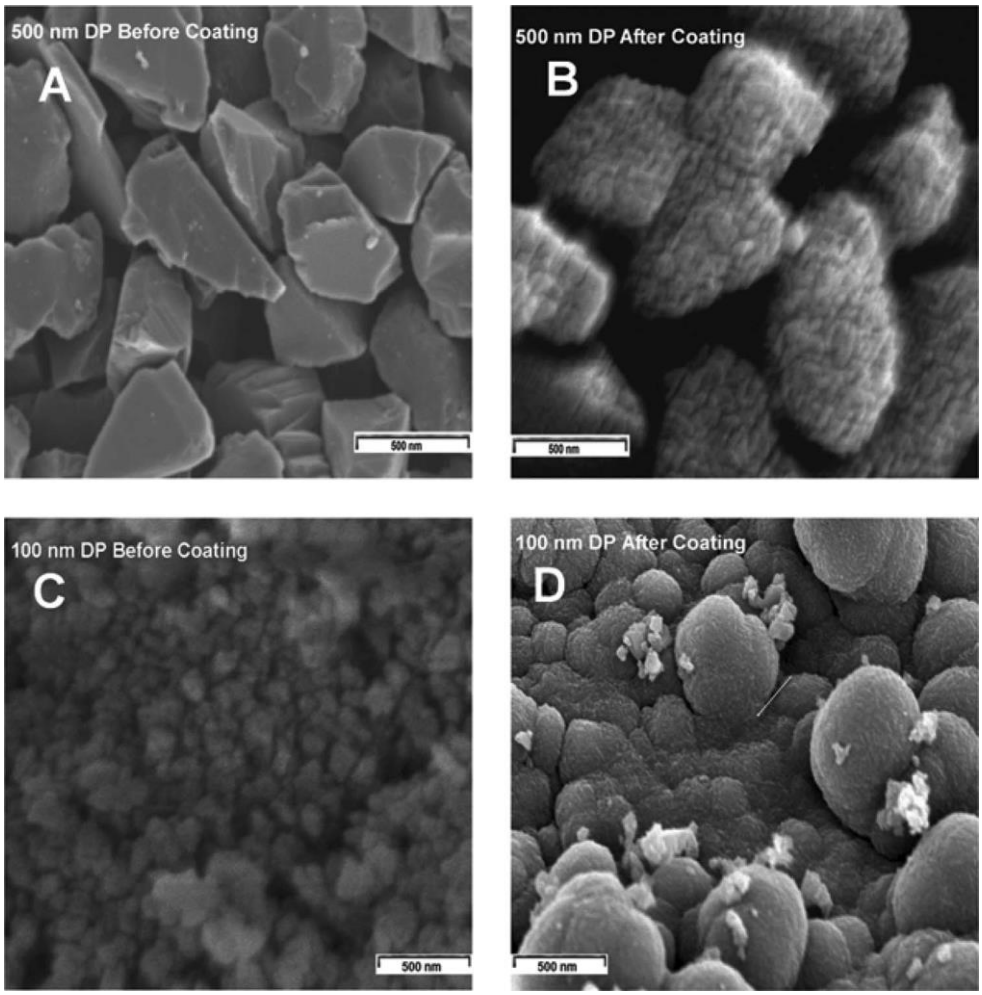

The as-received glassy carbon powder had a specific surface area of only 2 $m^2 g^{-1}$; nevertheless, its properties are important as they can help to understand the behavior of sp^2 carbon coated with a layer of BDD. Since Ar-rich gas mixtures were used in both papers, a high rate nucleation rate was achieved, leading to the deposition of BDD with small grain sizes. Additionally, it is possible to see in Figures 13 (B) and (D) and Figure 14 (B) that the BDD in this case has a

nodular morphology, typical of diamond grown in Ar-rich environments. A fundamental reason for the use of Ar-rich gas mixtures instead of the more traditional H-rich gas mixtures is the reduced rate of carbon gasification in the Ar-rich environment (KIM; MERZOUGUI; SWAIN, 2009). A high amount of hydrogen can be a problem when using sp^2 carbon substrates because of the high gasification rate that occurs in the presence of atomic hydrogen, leading to a significant mass loss. Regarding the morphology of the uncoated substrates, the uncoated diamond powder particles are irregularly shaped and have sharp, jagged edges, as shown in Figures 13 (A) and (C). In the case of the uncoated GC powders, as can be seen in Figure 14 (A), the surface is smooth and non-porous. In all cases, the diamond overlayer is easily seen by SEM.

Figure 14 - Scanning Electron Microscopy (SEM) images of **(A)** as-received GC powder, **(B)** coated B-UNCD-GC powder, and **(C)** coated B-UNCD-GC powders showing some incomplete diamond growth. Source: ref. (KIM; MERZOUGUI; SWAIN, 2009).

(A) **(B)**

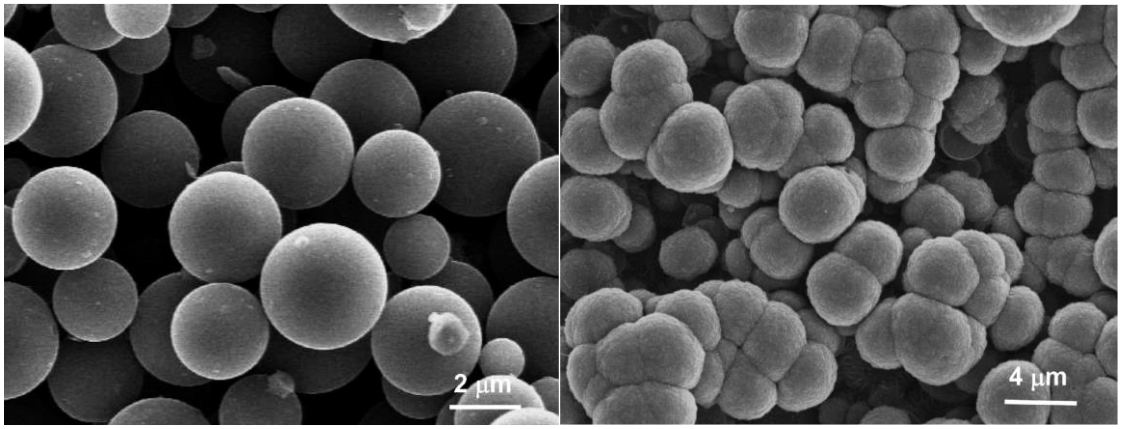

(C)

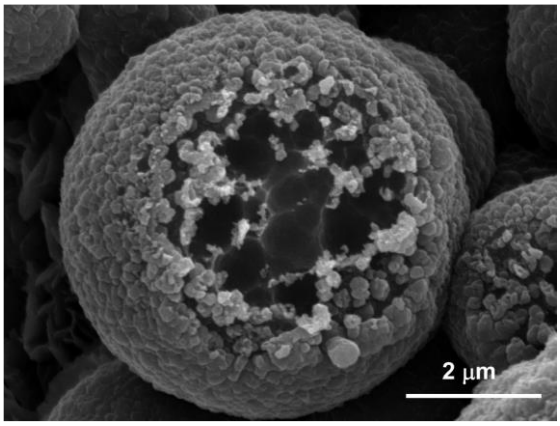

Diamond deposition on powders by CVD yields a high fraction of coated particles, although there are still some limitations to this approach (SHOW; SWOPE; SWAIN, 2009). Diamond growth connects neighboring particles, which leads to particle-particle fusion. This process, which can be seen in Figures 13 (B) and 14 (B), reduces the surface area of the powders. Additionally, not all the substrate particles are accessible to the reactive gas species, leading to incomplete diamond coverage, as can be seen in Figure 14 (C). Additionally, the temperature

of the substrate powder may also not be completely homogenous during the CVD process, due to the reactor design, which may lead to the deposition of other carbon structures besides diamond. A challenge with the use of CVD in the preparation of BDD powders using the core-shell approach is the balance between deposition time and synthesis conditions necessary to achieve maximal coating of the particles while avoiding considerable particle-particle fusion (AY, 2011).

4) Analysis of BDD with Raman Spectroscopy

Raman spectroscopy is a non-destructive spectroscopy technique widely used for the analysis of carbon materials. As any spectroscopy technique, Raman spectroscopy measures certain interactions of matter with light. Radiation from the near infrared (NIR) or ultraviolet range can interact with a molecule, leading to several types of scattering: Rayleigh, Stokes and anti-Stokes scattering – see Figure 15. In all types of scattering, a photon with $h\nu$ energy excites the molecule from a vibrational state to a virtual state. The molecule is then relaxed and may return to its original vibrational state, or to a higher or lower vibrational state, depending on the type of scattering. Raman spectroscopy measures the change in energy/wavenumber between the incident and scattered photons associated with Stokes and anti-Stokes transitions.

Figure 15 - Types of scattering by a molecule excited with a photon of energy equal to hν. Source: ref. (RAJA, PAVAN M. V. BARRON, 2020).

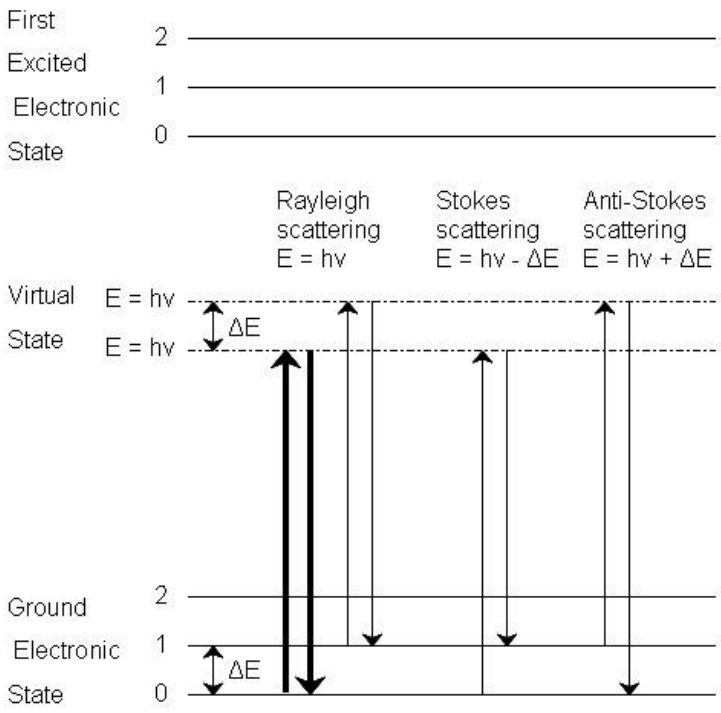

Carbon materials are strong Raman scatterers, with diamond and related materials having strong and easily identifiable Raman spectra (KNIGHT; WHITE, 1989). The spectrum of pure diamond (shown in Figure 16) is made of a single peak, which corresponds to the first order phonon mode of diamond. Pure diamond and BDD thin films show this peak at 1332 cm^{-1} with a full width at half maximum (FWHW) of around 10 cm^{-1} (XU; GRANGER; CHEN; STROJEK; LISTER; SWAIN, 1997). The line width is a qualitative indicator of crystalline film quality (BENNETT; WANG; SHOW; SWAIN, 2004). Crystals are arranged in a highly ordered pattern, but may present defects that are interruptions of this pattern. If more defects are present, the phonon lifetime is shorter, while the linewidth is longer. NCD has a broader linewidth than MCD, (SHOW; WITEK; SONTHALIA; SWAIN, 2003) 140 cm^{-1} versus 10 cm^{-1}. This is due to the smaller grain size and higher defect density in NCD films compared to MCD films.

Figure 16 - Raman spectrum of a diamond film. Source: ref. (SETASUWON; METANAWIN, 2009).

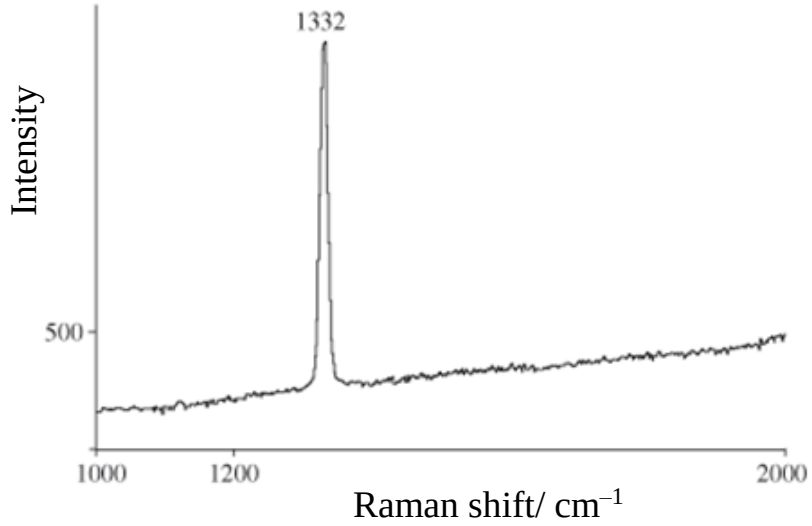

The diamond peak line width, as well as its position and other spectral features are very sensitive to the doping level (GRANGER; WITEK; XU; WANG; HUPERT; HANKS; KOPPANG; BUTLER; LUCAZEAU; MERMOUX; STROJEK; SWAIN, 2000). As the boron concentration increases, the diamond peak position shifts to lower wavenumbers and becomes asymmetrical, while its intensity decreases (BARTLETT; ALKIRE; LIPKOWSKI, 2015; LÉVY-CLÉMENT; NDAO; KATTY; BERNARD; DENEUVILLE; COMNINELLIS; FUJISHIMA, 2003). Its position is also known to shift with stress, the degree and direction of which are measures of stress magnitude and type, respectively (FISCHER; SWAIN, 2005). The intensity of the Raman spectrum can be related to the film thickness, (SHOW; SWOPE; SWAIN, 2009) as a thicker diamond film will lead to more photons being scattered and consequently a stronger signal. Regarding crystallite size, as it decreases, the material becomes more disordered and selection rules break down, which results in the broadening, shifting, and asymmetry of existing peaks and even occurrence of new peaks (BARTLETT; ALKIRE; LIPKOWSKI, 2015).

BDD has sp^2 impurities that lead to the appearance of two bands at 1350 and 1580 cm^{-1}, which correspond to the D and G bands, respectively – see Figure 17. The D band becomes active due to the presence of small crystallites or high amount of crystalline boundary, and follows the amount of edge plane or degree of microstructural disorder (MAY; ASHFOLD; MANKELEVICH, 2007). The G band is due to the first order scattering of crystalline graphite (sp^2 carbon) and involves an in-plane ring breathing mode (SHOW; SWOPE; SWAIN, 2009).

Figure 17 - Raman spectrum of a glassy carbon showing the D and G bands. Source: ref. (KIM; MERZOUGUI; SWAIN, 2009).

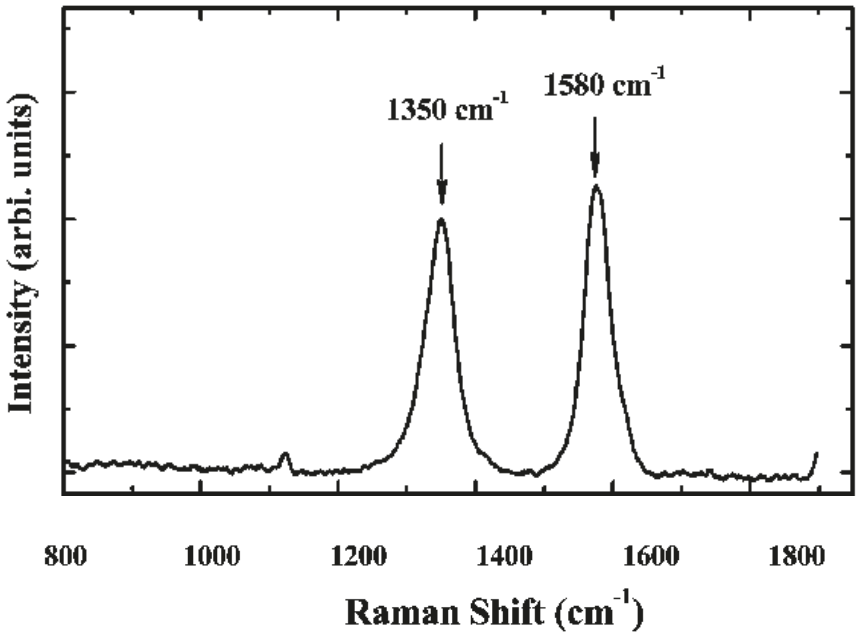

UNCD has a distinct spectrum, made up of the diamond peak, the D and G bands, as well as two other peaks at 1150 and 1470 cm^{-1}. Its spectrum consists therefore of bands at 1150, 1333, 1350, 1470, and 1550 cm^{-1}, as can be seen in Figure 18. The peaks at 1150 and 1470 cm^{-1} have been used to assess high quality UNCD and also have been the subject of controversy in the literature (KIM; MERZOUGUI; SWAIN, 2009). They have been attributed to *trans*-poly-acetelene fragments that lie in the grain boundaries of the diamond crystallites, (AYRES; NEWLAND; NEWTON; MANDAL; WILLIAMS; MACPHERSON,

2017) with the peak at 1150 cm^{-1} corresponding to the C-H bending of these fragments and the peak at 1470 cm^{-1} corresponding to C-C stretching (ARENAL; MONTAGNAC; BRUNO; GRUEN, 2007).

Figure 18 - Raman spectrum of a coated boron-doped UNCD glassy carbon powder. Source: ref. (KIM; MERZOUGUI; SWAIN, 2009).

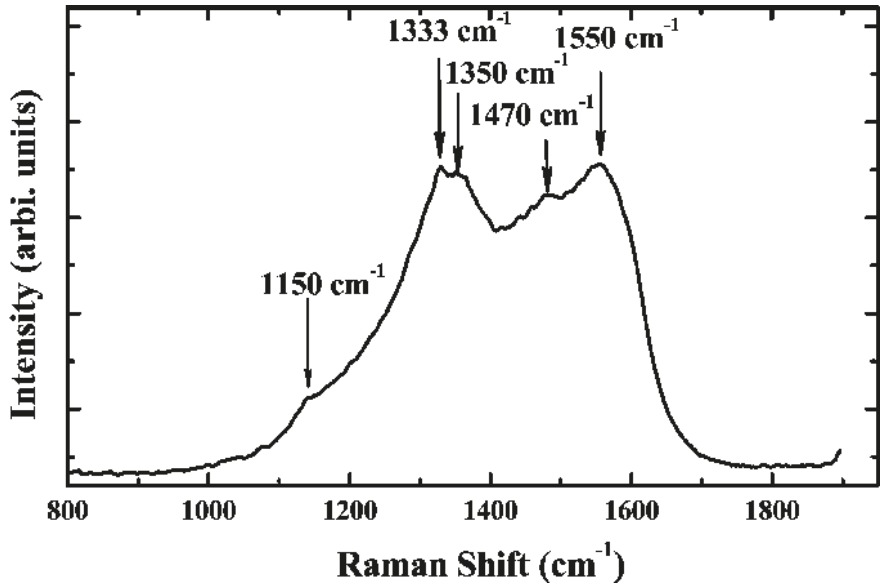

UNCD is made up of 50-100 nm nodules with diamond grains of approximately 10 nm, connected by sp^2 carbon at the grain boundaries, (AY, 2011; YANG; YU; MACPHERSON; EINAGA; ZHAO; ZHAO; SWAIN; JIANG, 2019) which leads to the appearance of the D and G bands. It is important to note that the Raman cross section for this sp^2 bonded carbon is around 50 times larger than that of sp^3 bonded carbon (KNIGHT; WHITE, 1989). Therefore, a relatively small amount of sp^2 carbon impurities can dominate the Raman spectrum. Nevertheless, the relative intensity of the sp^3 diamond peak and the sp^2 G band is commonly used as a qualitative estimation of the diamond material quality (MACPHERSON, 2015). These sp^2 carbon peaks can come not only from impurities within the diamond matrix, but also from an incomplete coating of the substrate, as can be seen in Figure 14 (C). In that case, GC was used as the substrate, with its spectrum consisting of the D and G bands, shown in Figure 17. Therefore,

an incomplete diamond coating could have led to scattering by the GC substrate and contributed to the appearance of the D and G bands.

Due to the high sensitivity of Raman spectroscopy to sp^2 bonded carbon, UNCD with an M-shaped Raman spectrum has been reported in the literature (ZENG; KONICEK; MOLDOVAN; MANGOLINI; JACOBS; WYLIE; ARUMUGAM; SIDDIQUI; CARPICK; CARLISLE, 2015). In this case, the D and G bands dominated this spectrum, which is usually thought to happen in the presence of a high amount of graphite and disordered carbon; however, Zeng *et al.* (ZENG; KONICEK; MOLDOVAN; MANGOLINI; JACOBS; WYLIE; ARUMUGAM; SIDDIQUI; CARPICK; CARLISLE, 2015) eliminated this possibility by conducting other analyses. Nevertheless, non-diamond carbon (NDC) can be oxidized as a way to remove these impurities. Detonation nanodiamond particles, for example, can be oxidized between 375-450 °C , which removes non-diamond carbon while avoiding significant loss of diamond (OSSWALD; YUSHIN; MOCHALIN; KUCHEYEV; GOGOTSI, 2006). This intuitively led to a significant increase in the intensity of the diamond peak. It is also important to note that laser wavelength influences the scattering sensitivity of sp^2 carbon relative to sp^3 carbon,(MACPHERSON, 2015) so it should be considered and mentioned when analyzing the relative sp^3/sp^2 ratio with Raman spectroscopy.

5) Electrochemistry of BDD

5.1) Cyclic Voltammetry

BDD is a possible electrocatalyst support material, with its physicochemical and electrochemical properties being of great interest as they provide information on how different types of BDD may behave in a PEMFC. Cyclic voltammetry is an electrochemical technique that allows one to obtain information such as potential limits, voltammetric features, background capacitance, and rate

constants and other electrochemical data for many redox analytes. These directly relate to the physicochemical properties of BDD as they are all sensitive to the microstructure, surface and electronic properties of the BDD electrode (AY, 2011).

When cyclic voltammetry is employed, the electrochemical cell usually consists of a working electrode, a counter electrode, and a reference electrode, immersed in an electrolytic solution. The potential of the working electrode is varied cyclically (x-axis) while the electric current is measured (y-axis), leading to the acquisition of a cyclic voltammogram (CV). If a redox analyte is used within the appropriate conditions, it may be oxidized and reduced depending on the potential of the working electrode, leading to the appearance of redox peaks. If no redox analyte is used, then a capacitive current may be observed due to the flow of electrolyte ions as a response to charge buildup in the working electrode; in this case, a background CV is obtained. The background CVs of BDD films are generally featureless, with low background currents (or capacitances) and show a wide working potential window (XU; GRANGER; CHEN; STROJEK; LISTER; SWAIN, 1997) – see Figure 19.

For a boron-doped NCD film, the background capacitance (C_{dl}) is about 4–7 μF cm^{-2} in aqueous solutions, (YANG; YU; MACPHERSON; EINAGA; ZHAO; ZHAO; SWAIN; JIANG, 2019) while it is ~30 μF cm^{-2} for Pt, Au, and GC (BARTLETT; ALKIRE; LIPKOWSKI, 2015; XU; GRANGER; CHEN; STROJEK; LISTER; SWAIN, 1997). C_{dl} is equal to i_{av}/nA, where i_{av} is the average current from the forward and reverse sweep, n is the scan rate, and A is the electrode area. The lower background capacitance of BDD is due to the lower density of potential-dependent electronic states and the absence of pseudocapacitance from electroactive surface carbon-oxygen functional groups (YANG; YU; MACPHERSON; EINAGA; ZHAO; ZHAO; SWAIN; JIANG, 2019). The absence of functional groups in the BDD surface also correlate with many other properties of BDD as will be shown below.

Figure 19 - Background CV (v = 100 mV s^{-1}) of a boron-doped NCD film in 1.0 mol L^{-1} KCl (A = 0.2 cm^2). Source: ref. (SHOW; WITEK; SONTHALIA; SWAIN, 2003).

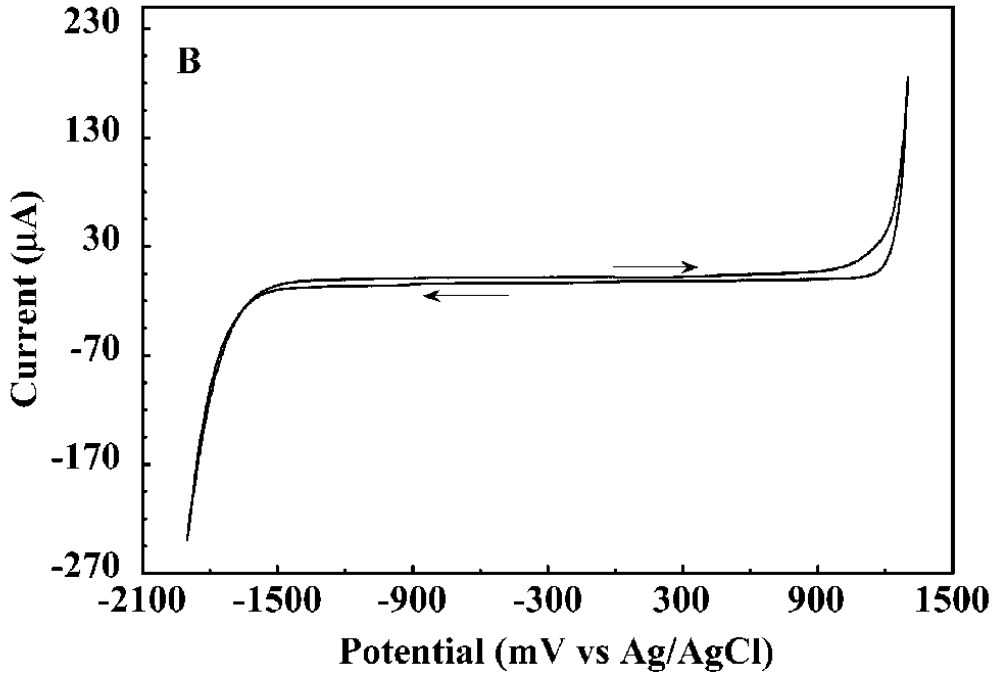

BDD has a working potential window of around 3.5 V, (XU; GRANGER; CHEN; STROJEK; LISTER; SWAIN, 1997) which is defined as the potential range in which the solvent is stable and will not be electrolyzed. This potential window will be dependent on the pH, on the electrolyte, on the current values used to define the potential window, (MACPHERSON, 2015) as well as on the specific type and quality of the BDD electrode. The wide potential window of BDD is due to the catalytically inert sp^3 carbon. Water electrolysis requires the presence of catalytic sites to be efficient, but with the lack of binding sites in the diamond surface, water electrolysis is hindered and thus the solvent window is wide (BARTLETT; ALKIRE; LIPKOWSKI, 2015).

NDC or sp^2 impurities have reactive sites that lead to the formation of carbon-oxygen functional groups and consequent appearance of some redox peaks (FISCHER; SWAIN, 2005). As previously discussed, these impurities tend

to form at the BDD grain boundaries and are most expressive in UNCD, which has a high amount of grain boundaries due to its small grain size. The resultant redox peaks from the carbon oxygen functionalities can be seen in Figure 20 (A) and are mainly due to the presence of the quinone/hydroquinone couple (SHOW; SWOPE; SWAIN, 2009) – depicted in Figure 20 (B). NDC can provide catalytic sites for water electrolysis, which leads to a reduction of the solvent window. Additionally, a higher background current may be observed in the presence of sp^2 carbon impurities due to a faradaic contribution from the NDC (SHOW; WITEK; SONTHALIA; SWAIN, 2003). Briefly put, the background current, the working potential window, and the voltammetric features are all affected and sensitive to the presence of NDC (GRANGER; WITEK; XU; WANG; HUPERT; HANKS; KOPPANG; BUTLER; LUCAZEAU; MERMOUX; STROJEK; SWAIN, 2000).

Figure 20 – **(A)** Background CV of boron-doped MCD containing negligible NDC (black line) and considerable NDC (purple line); **(B)** hydroquinone/quinone redox couple. Source of Fig. (A): ref. (MACPHERSON, 2015).

A) B)

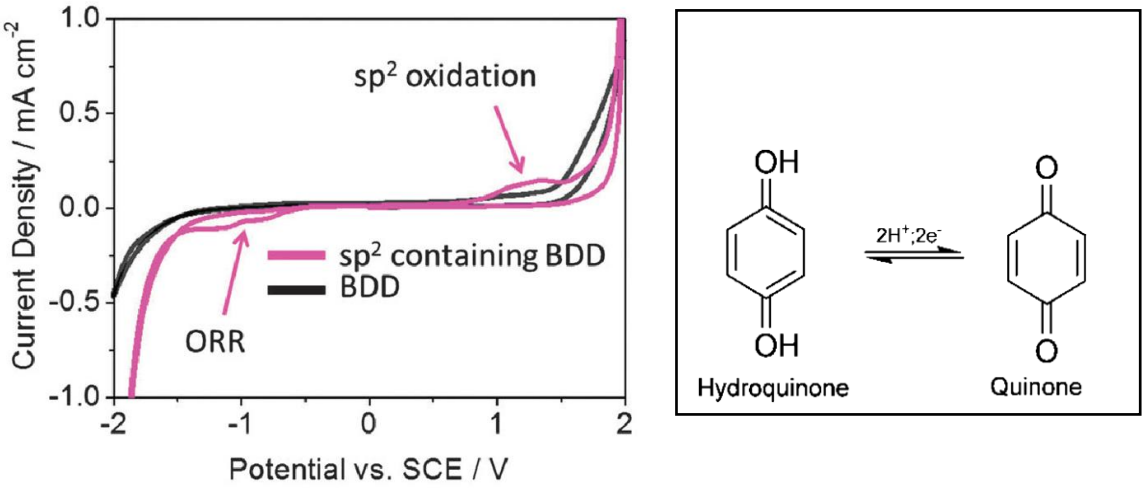

The same rationale can be applied to BDD coated powders. GC powder, a sp^2 carbon, when coated with a layer of BDD will present the electrochemical features of BDD. As can be seen in Figure 21 (A), the CV for as-received GC powder shows the quinone/hydroquinone redox peaks centered at around 0.4 V.

After coating the powder with boron-doped UNCD, the CV became featureless while the background current decreased due to the lower background capacitance of BDD (KIM; MERZOUGUI; SWAIN, 2009). In other cases, after close inspection, some redox peaks due to the carbon oxygen functionalities were observed even after coating the powders with BDD. These peaks can be seen in Figure 21 (B), where an insulating diamond powder (8–12 μm diameter, 2 m^2 g^{-1}) was coated with a layer of BDD, with deposition times from 1 to 6 h (FISCHER; SWAIN, 2005). These redox peaks are stronger for the 4 and 6 h growth BDD powders and are due to the NDC present in the grain boundaries, which can be formed during the CVD growth.

Figure 21 - Background CV of: **(A)** as-received GC and B-UNCD-GC powders; **(B)** diamond powders coated with a layer of BDD after different deposition times. Sources: (A) ref. (KIM; MERZOUGUI; SWAIN, 2009); (B) ref. (FISCHER; SWAIN, 2005).

A) B)

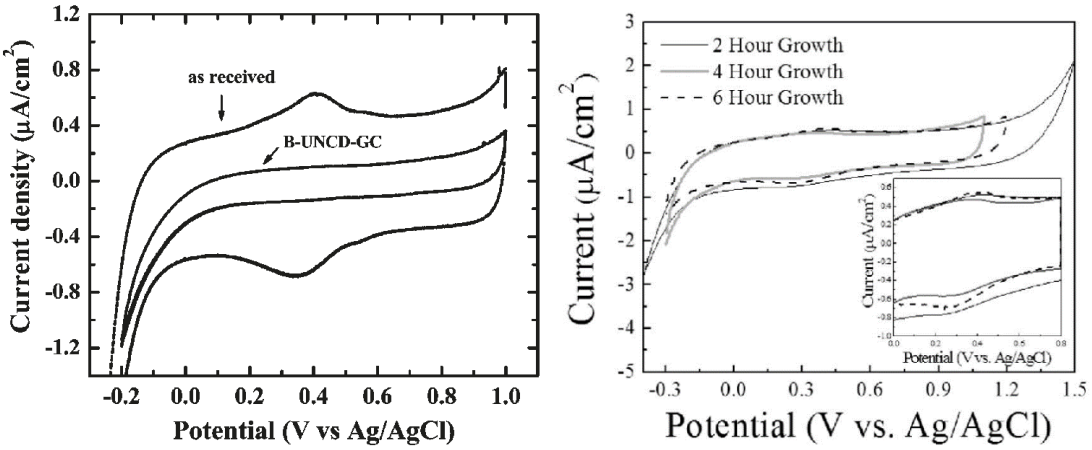

Raman spectroscopy can used to provide an indication of the presence of sp^2 carbon. For example, it is possible observe the sp^2 D and G peaks in the Raman spectrum of boron-doped UNCD. Despite this utility, Raman spectroscopy is relatively surface insensitive, as it provides information on the NDC content up to several microns from the surface (FERREIRA; ABRAMOF; CORAT;

TRAVA-AIROLDI, 2003). In electrochemical applications, charge-transfer processes occur at the surface and Raman spectroscopy may not give the relevant information on the NDC content. Concerning the surface quinone coverage, an electrochemical method is effective for characterizing sp^2 content as the electroactive quinone response directly correlates with the sp^2 surface carbon content (AYRES; NEWLAND; NEWTON; MANDAL; WILLIAMS; MACPHERSON, 2017). This surface NDC content can be removed with acid washing and rehydrogenation (GRANGER; WITEK; XU; WANG; HUPERT; HANKS; KOPPANG; BUTLER; LUCAZEAU; MERMOUX; STROJEK; SWAIN, 2000), leading to a change in the voltammetric features of the BDD electrode.

The redox systems shown in Table 1 are commonly used to characterize BDD electrodes. Their response is affected by factors such as (i) the dopant type, concentration and distribution, (ii) surface terminations and (iii) NDC impurities (YANG; YU; MACPHERSON; EINAGA; ZHAO; ZHAO; SWAIN; JIANG, 2019). Different electrochemical behavior can be observed for different BDD electrodes and redox analytes, therefore it is important to take into consideration the previously mentioned factors when interpreting electrochemical data. Rate constants can also vary and when the electron transfer (ET) rate constant is much greater than the diffusional rate constant, the CV is considered reversible as it is only limited by diffusion of the redox analyte (MACPHERSON, 2015). The heterogeneous ET rate constant can be highly influenced by the electrode surface cleanliness, electrolyte, and density of electronic states near the formal potential of the redox couple (AY, 2011).

Table 1 – Values of the heterogeneous electron rate constant (k^{o}_{app}) of commonly used redox analytes at BDD electrodes. Source: ref. (HUPERT; MUCK; WANG; STOTTER; CVACKOVA; HAYMOND; SHOW; SWAIN, 2003).

Redox couple	$\boldsymbol{k^{o}_{app}}$ **/ (cm s^{-1})**
$[Fe(CN)_6]^{3-/4-}$	0.01 – 0.1
$[Ru(NH_3)_6]^{3+/2+}$	0.01 – 0.1
$IrCl_6^{2-/3-}$	0.01 – 0.1
Methyl viologen (MV^{2+}/MV^{+})	0.01 – 0.1
4-*tert*-butylcatechol	10^{-6} – 10^{-4}
$Fe^{3+/2+}$	10^{-6} – 10^{-4}
Ferrocene	0.01 – 0.1

Redox reactions can be classified on two types based on how the observed redox analyte will undergo ET. In an outer-sphere reaction, the analyte will simply diffuse to electrode solution interface, with the electrode either acting as a source or sink for electrons. In this type of reaction, the reaction kinetics are relatively insensitive to the microstructure and surface chemistry of the electrode but are very sensitive to the density of electronic states near the formal potential (BENNETT; WANG; SHOW; SWAIN, 2004). In an inner-sphere reaction, however, there is a strong interaction between the redox species and the electrode surface, with these species being often specifically adsorbed on the surface (BARTLETT; ALKIRE; LIPKOWSKI, 2015). This type of reaction is therefore surface sensitive, with the rate of the reaction being highly influenced by the electrode material.

For inner-sphere reactions, more sluggish ET transfer kinetics are observed on BDD compared to sp^2 carbon or metal electrodes (e.g. Au, Pt) (YANG;

YU; MACPHERSON; EINAGA; ZHAO; ZHAO; SWAIN; JIANG, 2019). This is due to the electrocatalytically inert diamond surface, evidenced by its wide potential window, low background current, and featureless background CV. The $[Fe(CN)_6]^{3-/4-}$ redox couple, which undergoes inner-sphere ET, is one of the most studied redox systems on BDD and has variable results of ET constants due to its sensitivity to surface functional groups and NDC content (MACPHERSON, 2015). With BDD films, well-defined redox waves are observed (see example in Figure 22), with peak-to-peak separation (ΔE_p) values of around 63–88 mV and oxidation peak current to reduction peak current ratios (I_{ox}/I_{red}) of around 1.0 (BENNETT; WANG; SHOW; SWAIN, 2004; SHOW; WITEK; SONTHALIA; SWAIN, 2003; XU; GRANGER; CHEN; STROJEK; LISTER; SWAIN, 1997). I_{ox} values vary linearly with the (scan rate)$^{1/2}$ for scan rates in the range of 100–500 mV s^{-1}, indicating that the current is limited by semi-infinite linear diffusion of the reactant.

Figure 22 - CV for 0.1 mmol L^{-1} $[Fe(CN)_6]^{3-/4-}$ in 0.1 mol L^{-1} KCl with a BDD film. Source: ref. (XU; GRANGER; CHEN; STROJEK; LISTER; SWAIN, 1997).

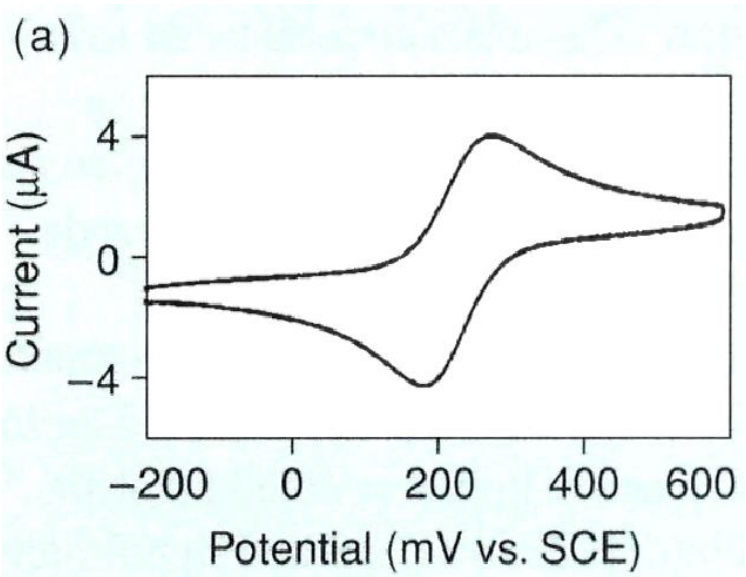

In the case of the 100 and 500 nm diamond powders coated with a layer of boron-doped NCD assessed with $[Fe(CN)_6]^{3-/4-}$ using a scan rate of 30 mV s^{-1} (AY; SWOPE; SWAIN, 2008), a larger ΔE_p value of 120 mV was observed for the 100 nm powder in comparison to a ΔE_p value of 76 mV for the 500 nm powder. Even though both powders showed similar conductivities, the larger peak splitting is attributed to ohmic resistance within the powder network, evidenced by a sloped background CV Regarding the diamond powder (8–12 µm diameter, 2 m^2 g^{-1}) coated with a layer of BDD, a distorted waveform was observed, with a large ΔE_p value of 143 mV at 10 mV s^{-1} or 348 mV at 500 mV s^{-1} (FISCHER; SWAIN, 2005). These ΔE_p values were also attributed to ohmic resistance effects, due to poor particle-particle contact revealed by SEM, with the diamond particles being irregularly shaped with jagged edges. The ohmic resistance within the diamond powder electrode increased with usage, apparently because of decreased connectivity between the particles (FISCHER; SWAIN, 2005).

For $[Ru(NH_3)_6]^{3+/2+}$, well defined redox waves were also observed using BDD films, with ΔE_p values in the range 60–93 mV and I_{ox}/I_{red} values of around 1.0 (BARTLETT; ALKIRE; LIPKOWSKI, 2015; BENNETT; WANG; SHOW; SWAIN, 2004; SHOW; SWOPE; SWAIN, 2009; SHOW; WITEK; SONTHALIA; SWAIN, 2003; XU; GRANGER; CHEN; STROJEK; LISTER; SWAIN, 1997). Additionally, the I_{ox} values indicate that the current is limited by semi-infinite linear diffusion of the reactant as well. The difference between $[Ru(NH_3)_6]^{3+/2+}$ and $[Fe(CN)_6]^{3-/4-}$ is that the former undergoes outer-sphere ET, with its kinetics relatively insensitive to the physicochemical properties of diamond (BENNETT; WANG; SHOW; SWAIN, 2004). They are mainly influenced by the density of electronic states at the formal potential of the redox system, (GRANGER; WITEK; XU; WANG; HUPERT; HANKS; KOPPANG; BUTLER; LUCAZEAU; MERMOUX; STROJEK; SWAIN, 2000; SHOW;

SWOPE; SWAIN, 2009; SHOW; WITEK; SONTHALIA; SWAIN, 2003) making $[Ru(NH_3)_6]^{3+/2+}$ useful for distinguishing between conducting and semi-conducting BDD, as the ET kinetics are strongly retarded at the semi-conducting electrode (YANG; YU; MACPHERSON; EINAGA; ZHAO; ZHAO; SWAIN; JIANG, 2019). Regarding the diamond powders, the same ohmic resistance effects were observed.

$Fe^{3+/2+}$ is a redox couple that undergoes inner-sphere ET, with its ET rate constant being very sensitive to surface carbon-oxygen functionalities, specifically carbonyl types, for both GC and diamond (BENNETT; WANG; SHOW; SWAIN, 2004). When the 500 nm diamond powder coated with a layer of boron-doped NCD was used to probe this redox couple, a large ΔE_p value of 221 mV was observed (AY; SWOPE; SWAIN, 2008). After acid washing and hydrogenation, an even larger value of 560 mV was observed, as can be seen in Figure 23. This increase in ΔE_p value is attributed to the loss of carbon-oxygen functionalities, which catalyze the redox reactions of the $Fe^{3+/2+}$ couple. Therefore, it is important to take into account the presence of NDC, as it can affect the cyclic voltammetry response by increasing the electrocatalytic activity and can also make a material appear more electrically conducting than it really is (MACPHERSON, 2015; YANG; YU; MACPHERSON; EINAGA; ZHAO; ZHAO; SWAIN; JIANG, 2019).

Figure 23 - CV (v = 30 mV s^{-1}) for 1.0 mmol L^{-1} $Fe^{3+/2+}$ in 0.1 mol L^{-1} $HClO_4$ with 500 nm diamond powder coated with a layer of BDD. Source: ref. (AY; SWOPE; SWAIN, 2008).

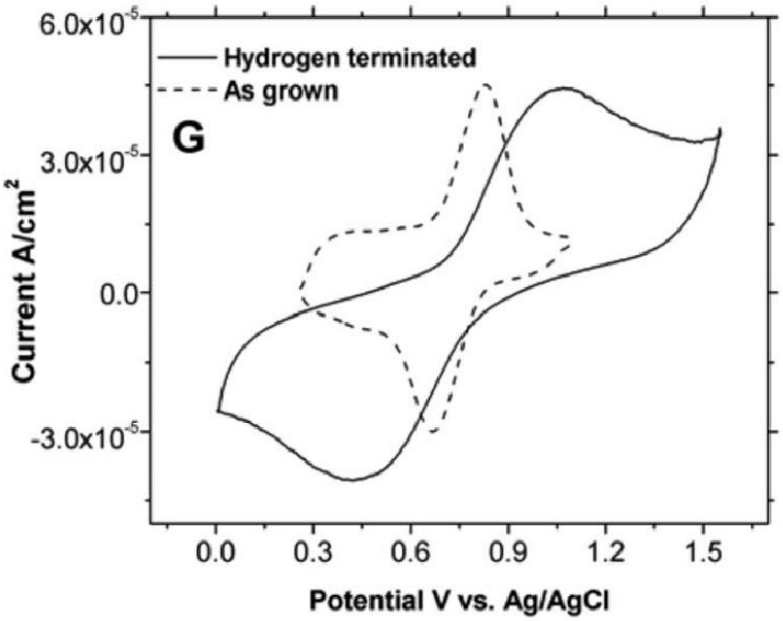

5.2) Durability and microstructural degradation of BDD powders

A viable PEMFC electrocatalyst support material needs to have a high corrosion resistance to withstand the corrosive environment within the PEMFC. The microstructural and dimensional stability of the BDD powders can be investigated through anodic polarization, by applying a potential of 1.4–1.6 V *vs*. Ag/AgCl in an acidic solution such as 0.5 mol^{-1} H_2SO_4, for 30–60 min at either room temperature (25 °C) or 80 °C (AY; SWOPE; SWAIN, 2008; FISCHER; SWAIN, 2005; KIM; MERZOUGUI; SWAIN, 2009). It is possible to observe that significantly less current passes through the diamond coated powders than through a GC powder – see Figure 24. The higher current for GC powder is consistent with more surface oxidation of this powder in comparison to the diamond

surface (KIM; MERZOUGUI; SWAIN, 2009). Additionally, it is possible to observe fluctuations in the current for GC powder, due to increases in the surface area of the powder as the particles degrade and corrode. This current and consequent oxidation of the GC powder result from a combination of carbon-oxygen functionalities formation, microstructural alteration, and corrosion in the form of gasification (AY; SWOPE; SWAIN, 2008). The corrosion rate of carbon materials is related to the degree of microstructural disorder, as more disordered materials have a higher corrosion rate (FISCHER; SWAIN, 2005). Since diamond is a crystalline material, its corrosion rate is much lower.

Figure 24: Amperometric *i vs. t* curves for 500 and 100 nm diamond powders coated with a layer of BDD recorded during anodic polarization at 1.4 V *vs.* Ag/AgCl and 80 °C for 1 h in 0.5 mol L^{-1} H_2SO_4. For comparison purposes, a curve for GC powder is also shown. Source: ref. (AY; SWOPE; SWAIN, 2008).

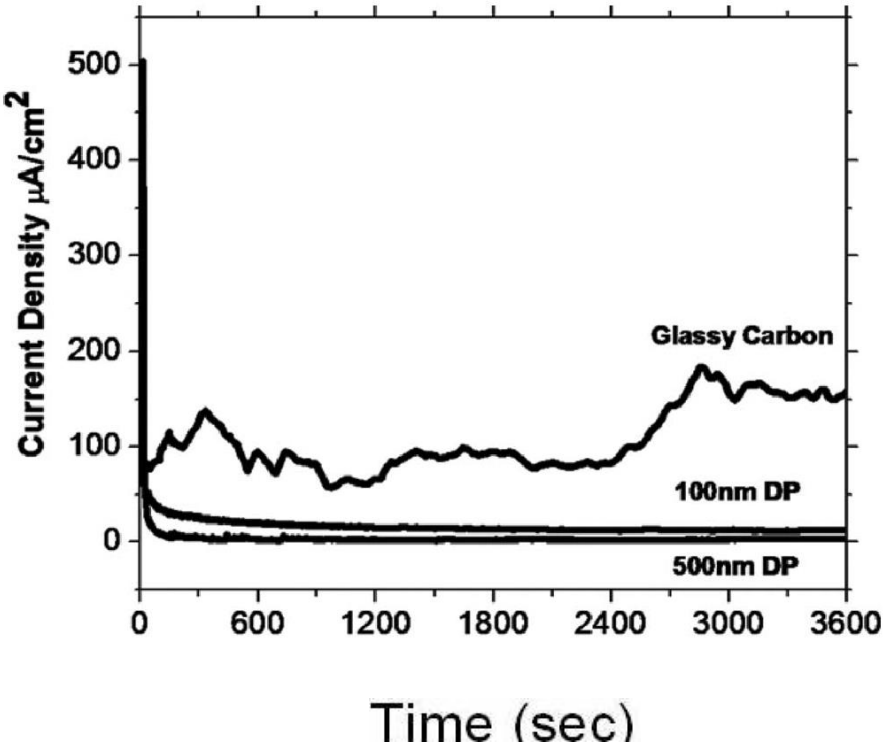

SEM can be complementarily used with the electrochemical data to verify the microstructural degradation of the powders. Thus, Figures 23 (a) and (b) show the GC powder before and after anodic polarization, respectively. It is possible to see a large number of broken or fractured particles, indicating that microstructural damage and corrosion of the carbon material occurred, likely leading to an increase in surface area. A B-UNCD-GC powder is apparently unchanged after anodic polarization, as can be seen in Figures 23 (c) and d). The electrochemical and SEM data show that coating the GC particles with a layer of B-UNCD imparts a high degree of dimensional stability and corrosion resistance to the material (KIM; MERZOUGUI; SWAIN, 2009).

Figure 25 - SEM images of GC powder (A) before and (B) after polarization at 1.6 V *vs.* Ag/AgCl for 30 min in 0.5 mol L^{-1} H_2SO_4 at a temperature of 80 °C. Images are also shown for a B-UNCD-GC powder (C) before and (D) after the same polarization. Source: ref. (KIM; MERZOUGUI; SWAIN, 2009).

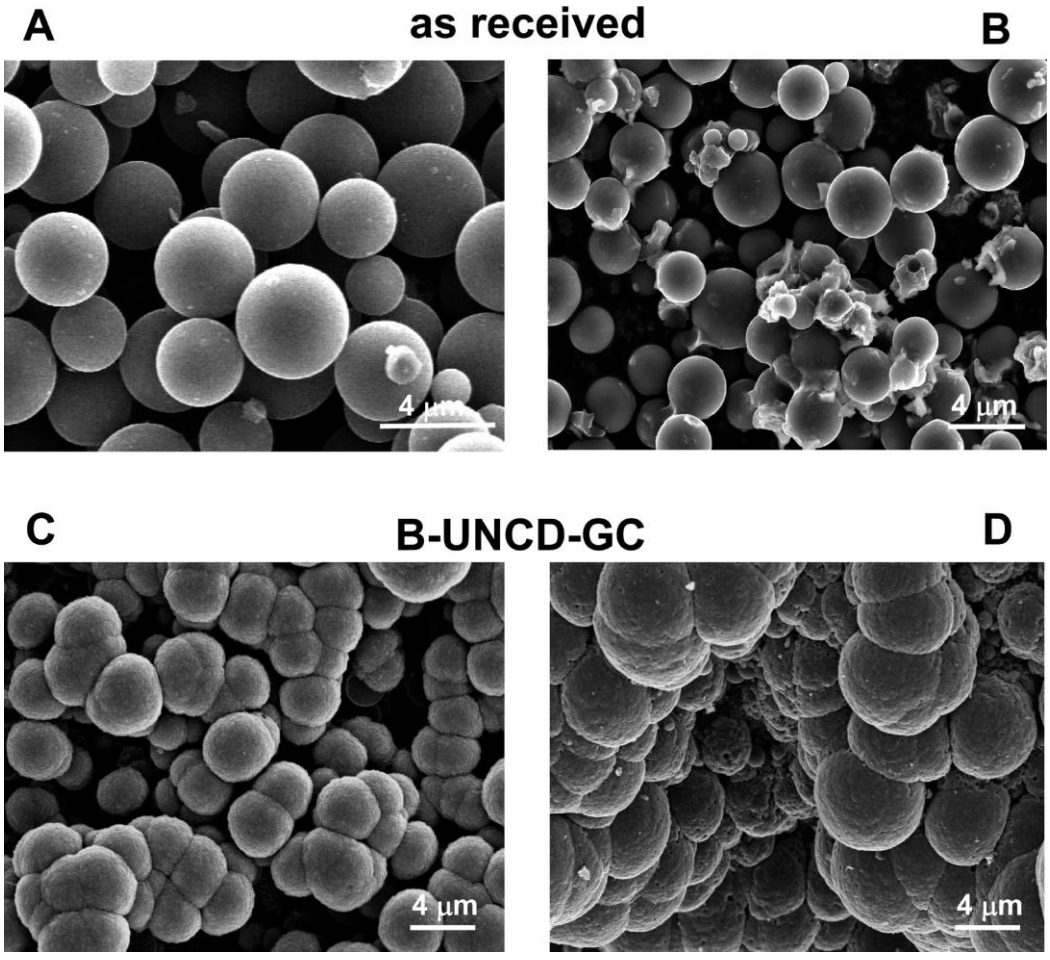

Cyclic voltammetry can also be used to verify the microstructural degradation of such powders, as the CV may change after anodic polarization. Diamond coated powders, due to their high corrosion resistance, show an unchanged CV after anodic polarization, indicating that no substantial change in their microstructure was made. In contrast, the CV for a GC powder is significantly changed after anodic polarization, as can be seen in Figure 26. Specifically, the peak and background currents increased after the anodic polarization. This is due to the formation of more functional groups associated to the microstructural degradation and corrosion of the GC surface (AY; SWOPE; SWAIN, 2008).

Figure 26 - CV of a GC powder before and after anodic polarization at 1.4 V *vs.* Ag/AgCl in 0.5 mol L^{-1} H_2SO_4 for 1 h at a temperature of 80 °C. Source: ref. (AY; SWOPE; SWAIN, 2008).

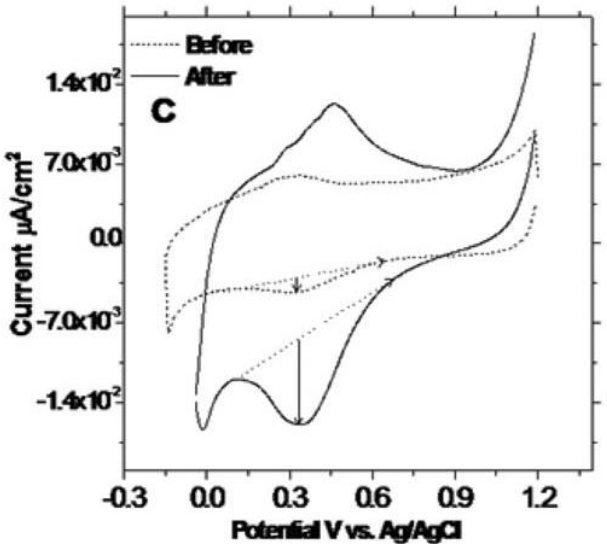

Carbon materials can be impregnated with Pt nanoparticles and studied electrochemically so their potential as an electrocatalyst support material can be better assessed. The CV of a Pt support (see Figure 27) is made of two peaks in the forward scan, one peak at around 0–0.25 V (*vs.* RHE) due to H desorp-

tion/oxidation, and another at 0.9 V, associated to Pt oxide formation. In the reverse scan, the peak at 0.6 V corresponds to the reduction of the Pt oxide, while the peak at 0–0.2 V represents H adsorption/reabsorption. Integration of part of the CV can be used to calculate the electrochemically active Pt surface area (ECSA), which is a very important parameter for fuel cell performance and durability. A large ECSA is associated to more catalytic sites for electrode reactions, better distribution of catalyst particles and favorable electrocatalyst-support material interaction (AY, 2011).

Figure 27 - CV in 0.1 mol L^{-1} $HClO_4$ for a Pt/B-UNCD-diamond powder (3–6 nm diameter). Dashed arrows show the increase in current response with scan number. Source: ref. (AY, 2011).

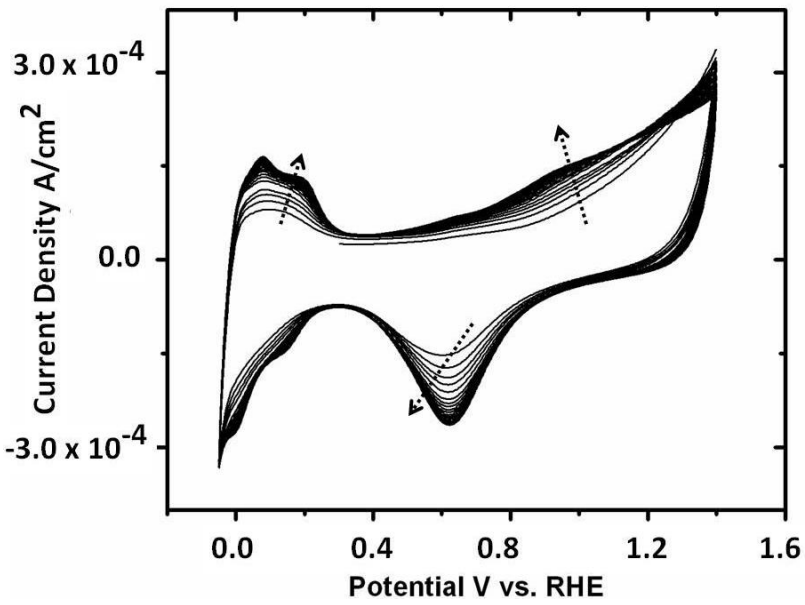

In comparison to the traditionally used Vulcan XC-72, nanodiamond BDD has been reported to have a higher ECSA (KIM; CHUN; LEE; LIM, 2015), while a B-UNCD-diamond powder presented a slightly lower ECSA (AY, 2011). Despite this difference, both studies found that the BDD powders have a higher corrosion resistance and durability than Vulcan XC-72. In the case of the platinized B-UNCD-diamond powder, its corrosion resistance was tested by anodic

polarization at 1.4 V *vs.* RHE in 0.5 mol L^{-1} H_2SO_4 for 1 h at 80 °C. As can be seen in Figure 28, the B-UNCD-diamond powder shows 83% less corrosion than Vulcan XC-72 in the same conditions (AY, 2011). Cyclic voltammetry was also performed after anodic polarization, with the typical features of Pt seen in Figure 27 being observed for the Pt/B-UNCD-diamond powder. The ECSA of this powder and of Pt/Vulcan XC-72 decreased after anodic polarization, however the decrease for the Pt/B-UNCD-diamond powder was much smaller, due to its higher corrosion resistance.

Figure 28 - Chronoamperometric *i vs. t* curves for **(A)** 20% (*m*/*m*) Pt/Vulcan XC-72, **(B)** Vulcan XC-72, **(C)** 20% (*m*/*m*) Pt/B-UNCD-diamond, and **(D)** B-UNCD, measured at 1.4 V *vs.* RHE 80 °C in N_2 purged 0.5 mol L^{-1} H_2SO_4. Source: ref. (AY, 2011).

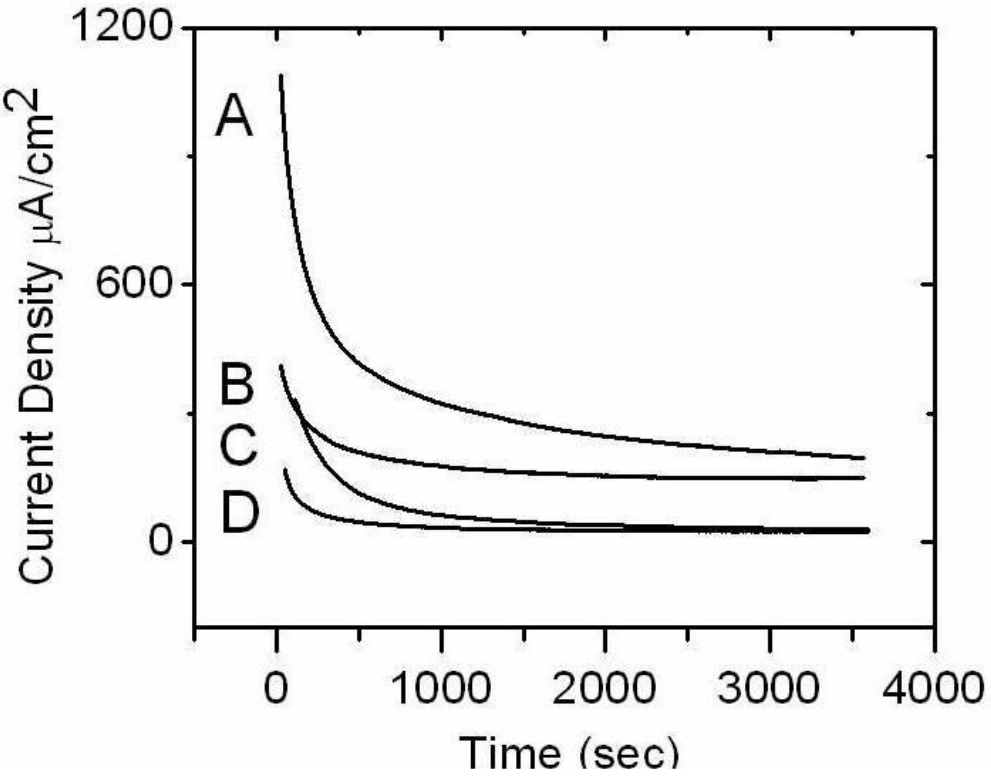

Accelerated long-term stability tests for 100 h of cell operation with Pt nanoparticles supported on nanodiamond BDD, Vulcan XC-72, and multi-walled carbon nanotubes (MWCNTs) were reported (KIM; CHUN; LEE; LIM,

2015). During these tests, a voltage of 0.6 V was maintained, the unit cells were kept at 90 °C, which is higher than the usual temperature for a PEMFC (70–80 °C), and a flow of H_2 and air was supplied. After 100 h of operation, the authors reported (as evidenced by SEM micrographs) that the surface of the BDD support was significantly less damaged than those of the MWNCTs and Vulcan XC-72 supports. This means that the BDD support would prevent Pt particle detachment and consequently reduce a decrease in cell performance. To verify this, energy dispersive X-ray (EDX) analysis was used to analyze the degradation of the Pt loading on the different catalysts by determining the composition of the supports after the accelerated long-term stability tests. As can be seen in Figure 29, the amount of Pt was reduced by 60% and 70% on the MWCNTs and Vulcan XC-72 catalysts after 60 min of operation, respectively, while on the BDD support it was only reduced by 30%. This shows that the Pt detachment is indeed less severe on the BDD support.

Figure 29 - Degradation of the Pt loading on different catalysts (indicated in the figure) as a function of time during an accelerated long-term stability test. Source: ref. (KIM; CHUN; LEE; LIM, 2015).

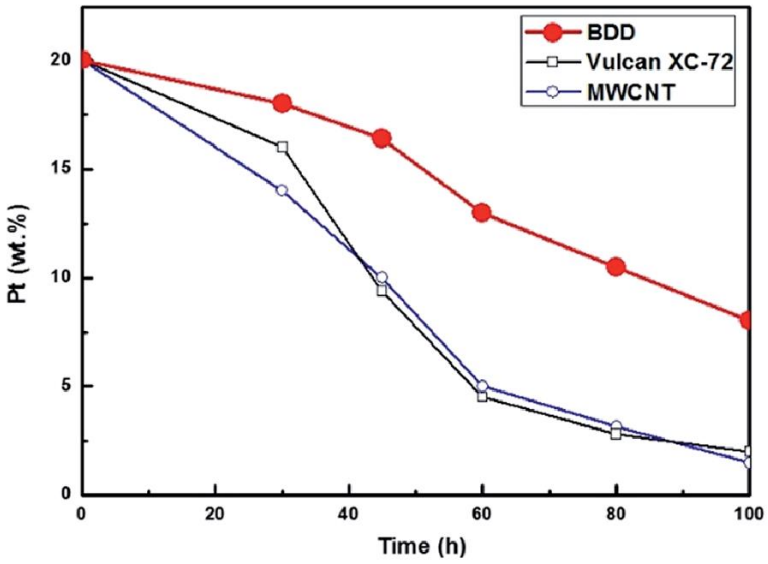

Conclusions

Degradation of the electrocatalyst support is a serious problem deterring large-scale implementation of PEMFCs. BDD is an interesting candidate for use as a support material in PEMFCs due to the attractive properties of diamond, particularly its high chemical stability and corrosion resistance. CVD is the most used method used for producing BDD, as it is consistent and allows control of the BDD properties. Reactor conditions, such as source gas mixture ratios, lead to different grain sizes, boron dopant incorporation and amounts of NDC content. UNCD, for example, is usually synthesized with Ar-rich gas mixtures and is made up of small grains, which lead to a relatively high amount of NDC that is present in the grain boundaries. BDD can be produced as film or as particles, with the latter being of more interest as a possible PEMFC support material due to their higher surface area. BDD particles can be produced via a core-shell approach; however, finding the balance between deposition time and synthesis conditions necessary to achieve maximal coating of the particles while avoiding considerable particle-particle fusion is a considerable challenge. For the analysis of the BDD microstructure, Raman spectroscopy is a valuable tool as it provides information on the crystalline quality and relative sp^2/sp^3 carbon ratios. UNCD has a Raman spectrum that has several peaks associated with NDC, such as the D and G peaks. Nevertheless, it is important to note that due to the higher Raman cross section of sp^2 carbon, Raman spectroscopy is much more sensitive to this type of carbon. The amount of NDC is an important parameter to be considered and assessed, since the electrochemical and physicochemical properties of BDD are related to sp^2 content; more NDC leads to a narrower potential window and is associated with increased surface oxidation. In background cyclic voltammetry, higher NDC content is associated with the presence of redox peaks, due to carbon-oxygen functionalities that form in the presence of these impurities. When certain redox probes such as $[Ru(NH_3)_6]^{3+/2+}$ and $[Fe(CN)_6]^{3-/4-}$ are used, well-defined redox waves are observed and I_{ox} values varies linearly with $(\text{scan rate})^{1/2}$, indicating that

the current is limited by semi-infinite linear diffusion of the reactant. These redox couples can be used to assess BDD properties, such as the NDC content and conductivity. For example, higher ΔE_p values are observed in powders with poor particle-particle contact, which leads to ohmic resistance within the powder network. $Fe^{2+/3+}$ can provide information on the NDC content, as its ET kinetics are highly sensitive to carbon-oxygen functional groups. Anodic polarization showed that the BDD particles present a smaller current than sp^2 carbon materials, which is consistent with the high corrosion resistance of diamond. Additionally, SEM images showed the BDD particles remain relatively unchanged after the anodic polarization while the sp^2 carbon materials underwent extensive microstructural damage. When the BDD particles and sp^2 carbon materials were impregnated with Pt nanoparticles, the same results were obtained with anodic polarization, i.e. the sp^2 carbon materials had higher currents due to more extensive surface oxidation. The accelerated long-term stability tests of the Pt supported on the different materials revealed the same trend, with the Pt nanoparticles supported on BDD presenting significantly less damage. Additionally, these nanoparticles presented less detachment than the Pt nanoparticles supported on sp^2 carbon, indicating that BDD has a superior durability than the sp^2 carbon materials. After careful analysis of the data reviewed in this work, it is possible to conclude that BDD powders have the potential of being an excellent electrocatalyst support material, due to their corrosion resistance and durability being higher than that of conventional sp^2 carbon materials.

References

ALASWAD, A.; DASSISTI, M.; PRESCOTT, T.; OLABI, A. G. Technologies and developments of third generation biofuel production. **Renewable and Sustainable Energy Reviews**, v. 51, p. 1446–1460, 2015.

ARENAL, R.; MONTAGNAC, G.; BRUNO, P.; GRUEN, D. M. Multiwavelength Raman spectroscopy of diamond nanowires present in n-type ultrananocrystalline films. **Physical Review B - Condensed Matter and Materials Physics**, v. 76, n. 24, p. 245316, 2007.

AY, A. **Boron Doped Ultrananocrystalline Diamond Powder: Alternative Support Material for PEMFCs**. [s.l.] Michigan State University, 2011.

AY, A.; SWOPE, V. M.; SWAIN, G. M. The physicochemical and electrochemical properties of 100 and 500 nm diameter diamond powders coated with boron-doped nanocrystalline diamond. **Journal of the Electrochemical Society**, v. 155, n. 10, p. B1013–B1022, 2008.

AYRES, Z. J.; NEWLAND, J. C.; NEWTON, M. E.; MANDAL, S.; WILLIAMS, O. A.; MACPHERSON, J. V. Impact of chemical vapour deposition plasma inhomogeneity on the spatial variation of sp^2 carbon in boron doped diamond electrodes. **Carbon**, v. 121, p. 434–442, 2017.

BALMER, R. S.; BRANDON, J. R.; CLEWES, S. L.; DHILLON, H. K.; DODSON, J. M.; FRIEL, I.; INGLIS, P. N.; MADGWICK, T. D.; MARKHAM, M. L.; MOLLART, T. P.; PERKINS, N.; SCARSBROOK, G. A.; TWITCHEN, D. J.; WHITEHEAD, A. J.; WILMAN, J. J.; WOOLLARD, S. M. Chemical vapour deposition synthetic diamond: Materials, technology and applications. **Journal of Physics Condensed Matter**, v. 21, n. 36, p. 364221, 2009.

BARBIR, F. PEM Fuel Cells: Theory and Practice. In: SAMMES, N. (Ed.). **Fuel Cell Technology: Reaching Towards Coomercialization**. London: Springer-Verlag, 2006. p. 27–51.

BARTLETT, P. N.; ALKIRE, R. C.; LIPKOWSKI, J. **Electrochemistry of Carbon Electrodes**. Weinheim, Germany: Wiley-VCH, 2015.

BENNETT, J. A.; WANG, J.; SHOW, Y.; SWAIN, G. M. Effect of sp2-bonded nondiamond carbon impurity on the response of boron-doped polycrystalline diamond thin-film electrodes. **Journal of the Electrochemical Society**, v. 151, n. 9, p. E306–E313, 2004.

BLOOMER, B. J.; STEHR, J. W.; PIETY, C. A.; SALAWITCH, R. J.; DICKERSON, R. R. Observed relationships of ozone air pollution with temperature and emissions. **Geophysical Research Letters**, v. 36, n. 9, p. L09803, 2009.

BOUCHAMA, A.; DEHBI, M.; MOHAMED, G.; MATTHIES, F.; SHOUKRI, M.; MENNE, B. Prognostic factors in heat wave–related deaths: A meta-analysis. **Archives of Internal Medicine**, v. 167, n. 20, p. 2170–2176, 2007.

BURKE, M.; DAVIS, W. M.; DIFFENBAUGH, N. S. Large potential reduction in economic damages under UN mitigation targets. **Nature**, v. 557, n. 7706, p. 549–553, 2018.

BURNS, D. A.; AHERNE, J.; GAY, D. A.; LEHMANN, C. M. B. Acid rain and its environmental effects: Recent scientific advances. **Atmospheric Environment**, v. 146, p. 1–4, 2016.

CASTANHEIRA, L.; DUBAU, L.; MERMOUX, M.; BERTHOME, G.; CAQUE, N.; ROSSINOT, E.; CHATENET, M. Carbon corrosion in proton-exchange membrane fuel cells: From model experiments to real-life operation in membrane electrode assemblies. **ACS Catalysis**, v. 4, p. 2258–2267, 2014.

CASTANHEIRA, L.; SILVA, W. O.; LIMA, F. H. B.; CRISCI, A.; DUBAU, L.; SA, C. P. Carbon corrosion in proton-exchange membrane fuel cells: Effect of the carbon structure, the degradation protocol, and the gas atmosphere. **ACS Catalysis**, v. 5, p. 2184–2194, 2015.

CHUNG, S.; HAM, K.; KANG, S.; JU, H.; LEE, J. Enhanced corrosion tolerance and highly durable ORR activity by low Pt electrocatalyst on unique pore structured CNF in PEM fuel cell. **Electrochimica Acta**, v. 348, p. 136346, 2020.

CIANCONI, P.; BETRÒ, S.; JANIRI, L. The impact of climate change on mental health: A systematic descriptive review. **Frontiers in Psychiatry**, v. 11, p. 74, 6 mar. 2020.

CIPRIANI, G.; DI DIO, V.; GENDUSO, F.; LA CASCIA, D.; LIGA, R.; MICELI, R.; RICCO GALLUZZO, G. Perspective on hydrogen energy carrier and its automotive applications. **International Journal of Hydrogen Energy**, v. 39, n. 16, p. 8482–8494, 2014.

DAS, H. S.; TAN, C. W.; YATIM, A. H. M. Fuel cell hybrid electric vehicles: A review on power conditioning units and topologies. **Renewable and Sustainable Energy Reviews**, v. 76, p. 268–291, 2017.

DAWSON, J. P.; BLOOMER, B. J.; WINNER, D. A.; WEAVER, C. P. Understanding the meteorological drivers of U.S. particulate matter concentrations in a changing climate. **Bulletin of the American Meteorological Society**, v. 95, n. 4, p. 521–532, 2013.

DEBE, M. K. Electrocatalyst approaches and challenges for automotive fuel cells. **Nature**, v. 486, n. 7401, p. 43–51, 2012.

DICKS, A. L. The role of carbon in fuel cells. **Journal of Power Sources**, v. 156, n. 2, p. 128–141, 2006.

DIFFENBAUGH, N. S.; BURKE, M. Global warming has increased global economic inequality. **Proceedings of the National Academy of Sciences of the United States of America**, v. 116, n. 20, p. 9808–9813, 2019.

DIJK, M.; ORSATO, R. J.; KEMP, R. The emergence of an electric mobility trajectory. **Energy Policy**, v. 52, p. 135–145, 2013.

DODGEN, D.; DONATO, D.; KELLY, N.; LA GRECA, A.; MORGANSTEIN, J.; RESER, J.; RUZEK, J.; SCHWEITZER, S.; SHIMAMOTO, M. M.; THIGPEN TART, K.; URSANO, R. Mental Health and Well-Being. In: **The Impacts of Climate Change on Human Health in the United States: A Scientific Assessment**. Washington, DC: U.S. Global Change Research Program, 2016. p. 217–246.

DU, L.; SHAO, Y.; SUN, J.; YIN, G.; LIU, J.; WANG, Y. Advanced catalyst supports for PEM fuel cell cathodes. **Nano Energy**, v. 29, p. 314–322, 2016.

EHSANI, M.; GAO, Y.; LONGO, S.; EBRAHIMI, K. **Modern Electric, Hybrid Electric, and Fuel Cell Vehicles**. 3ª. ed. Boca Raton: Taylor and Francis Group, 2018.

FANG, B.; KIM, J. H.; LEE, C.; YU, J. Hollow macroporous core/mesoporous shell carbon with a tailored structure as a cathode electrocatalyst support for proton exchange membrane fuel cells. **Journal of Physical Chemistry C**, v. 112, p. 639–645, 2008.

FANN, N.; BRENNAN, T.; DOLWICK, P.; GAMBLE, J. L.; ILACQUA, V.; KOLB, L.; NOLTE, C. G.; SPERO, T. L.; ZISKA, L. Air Quality Impacts. In: **The Impacts of Climate Change on Human Health in the United States: A Scientific Assessment**. Washington, DC: U.S. Global Change Research Program, 2016. p. 69–98.

FERREIRA, N. G.; ABRAMOF, E.; CORAT, E. J.; TRAVA-AIROLDI, V. J. Residual stresses and crystalline quality of heavily boron-doped diamond films analysed by micro-Raman spectroscopy and X-ray diffraction. **Carbon**, v. 41, n. 6, p. 1301–1308, 2003.

FIGUERES, C.; LE QUERE, C.; MAHINDRA, A.; BATE, O.; WHITEMAN, G.; PETERS, G.; GUAN, D. Emissions are still rising: ramp ut the cuts. **Nature**, v. 564, 2018.

FIGUERES, C.; SCHELLNHUBER, J. H.; WHITEMAN, G.; ROCKSTRÖM, J.; HOBLEY, A.; RAHMSTORF, S. Three years to safeguard our climate. **Nature**, v. 546, p. 593–595, 2017.

FISCHER, A. E.; SWAIN, G. M. Preparation and characterization of boron-doped diamond powder. **Journal of the Electrochemical Society**, v. 152, p. B369–B375, 2005.

GRANGER, M. C.; WITEK, M.; XU, J.; WANG, J.; HUPERT, M.; HANKS, A.; KOPPANG, M. D.; BUTLER, J. E.; LUCAZEAU, G.; MERMOUX, M.; STROJEK, J. W.; SWAIN, G. M. Standard electrochemical behavior of high-quality, boron-doped polycrystalline diamond thin-film electrodes. **Analytical Chemistry**, v. 72, n. 16, p. 3793–3804, 2000.

HSIANG, S. M.; BURKE, M.; MIGUEL, E. Quantifying the influence of climate on human conflict. **Science**, v. 341, n. 6151, p. 1235367, 2013.

HUPERT, M.; MUCK, A.; WANG, J.; STOTTER, J.; CVACKOVA, Z.; HAYMOND, S.; SHOW, Y.; SWAIN, G. M. Conductive diamond thin-films in electrochemistry. **Diamond and Related Materials**, v. 12, n. 10, p. 1940–1949, 2003.

Illustration of single crystal, polycrystalline and amorphous solids. Disponível em: <https://images.app.goo.gl/jXp9egE2gjsSLPTz9>.

International Energy Outlook 2019. Washington, DC: [s.n.]. Disponível em: <https://www.eia.gov/>.

KIM, D. Y.; MERZOUGUI, B.; SWAIN, G. M. Preparation and characterization of glassy carbon powder modified with a thin layer of boron-doped ultrananocrystalline diamond. **Chemistry of Materials**, v. 21, n. 13, p. 2705–2713, 2009.

KIM, J.; CHUN, Y. S.; LEE, S. K.; LIM, D. S. Improved electrode durability using a boron-doped diamond catalyst support for proton exchange membrane

fuel cells. **RSC Advances**, v. 5, n. 2, p. 1103–1108, 2015.

KNIGHT, D. S.; WHITE, W. B. Characterization of diamond films by Raman spectroscopy. **Journal of Materials Research**, v. 4, n. 2, p. 385–393, 1989.

LANGBROEK, J. H. M.; FRANKLIN, J. P.; SUSILO, Y. O. The effect of policy incentives on electric vehicle adoption. **Energy Policy**, v. 94, p. 94–103, 2016.

LE, A.; SMATTI, A. On the comparison and the complementarity of batteries and fuel cells for electric driving. **International Journal of Hydrogen Energy**, v. 39, n. 31, p. 17873–17883, 2014.

LÉVY-CLÉMENT, C.; NDAO, N. A.; KATTY, A.; BERNARD, M.; DENEUVILLE, A.; COMNINELLIS, C.; FUJISHIMA, A. Boron doped diamond electrodes for nitrate elimination in concentrated wastewater. **Diamond and Related Materials**, v. 12, n. 3, p. 606–612, 2003.

LÖW, P. **Hurricanes cause record losses in 2017 - The year in figures**. [s.l: s.n.]. Disponível em: <https://www.munichre.com/topics-online/en/climate-change-and-natural-disasters/natural-disasters/2017-year-in-figures.html>.

MACPHERSON, J. V. A practical guide to using boron doped diamond in electrochemical research. **Physical Chemistry Chemical Physics**, v. 17, p. 2935–2949, 2015.

MAJLAN, E. H.; ROHENDI, D.; DAUD, W. R. W.; HUSAINI, T.; HAQUE, M. A. Electrode for proton exchange membrane fuel cells : A review. **Renewable and Sustainable Energy Reviews**, v. 89, p. 117–134, 2018.

MASSON-DELMOTTE, V.; ZHAI, P.; PÖRTNER, H. O.; ROBERTS, D.; SKEA, J.; SHUKLA, P. R.; PIRANI, A.; MOUFOUMA-OKIA, W.; PÉAN, C.; PIDCOCK, R.; CONNORS, S.; MATTHEWS, J. B. .; CHEN, Y.; ZHOU, X.; GOMIS, M. I.; LONNOY, E.; MAYCOCK, T.; TIGNOR, M.; WATERFIELD, T. Summary for Policymakers**. In: Global Warming of 1.5°C. An IPCC**

Special Report on the impacts of global warming of 1.5°C above pre-industrial levels and related global greenhouse gas emission pathways, in the context of strengthening the global response toWorld Meteorological Organization. Geneva, Switzerland: [s.n.]. Disponível em: <http://www.ipcc.ch/report/sr15/>.

MATTUCI. **Proton-exchange membrane fuel cell**. Disponível em: <https://en.wikipedia.org/wiki/Proton-exchange_membrane_fuel_cell>.

MAY, P. W.; ASHFOLD, M. N. R.; MANKELEVICH, Y. A. Microcrystalline, nanocrystalline, and ultrananocrystalline diamond chemical vapor deposition: Experiment and modeling of the factors controlling growth rate, nucleation, and crystal size. **Journal of Applied Physics**, v. 101, n. 5, p. 053115, 2007.

MAY, P. W.; HARVEY, J. N.; SMITH, J. A.; MANKELEVICH, Y. A. Reevaluation of the mechanism for ultrananocrystalline diamond deposition from $Ar/CH_4/H_2$ gas mixtures. **Journal of Applied Physics**, v. 99, n. 10, p. 104907, 2006.

MAY, P. W.; LUDLOW, W. J.; HANNAWAY, M.; HEARD, P. J.; SMITH, J. A.; ROSSER, K. N. Raman and conductivity studies of boron-doped microcrystalline diamond, facetted nanocrystalline diamond and cauliflower diamond films. **Diamond and Related Materials**, v. 17, n. 2, p. 105–117, 2008.

MUNEER, T.; MILLIGAN, R.; SMITH, I.; DOYLE, A.; POZUELO, M.; KNEZ, M. Energetic, environmental and economic performance of electric vehicles: Experimental evaluation. **Transportation Research Part D**, v. 35, n. Complete, p. 40–61, 2015.

NEWBERY, D.; STRBAC, G. What is needed for battery electric vehicles to become socially cost competitive? **Economics of Transportation**, v. 5, p. 1–11, 2016.

OSSWALD, S.; YUSHIN, G.; MOCHALIN, V.; KUCHEYEV, S. O.;

GOGOTSI, Y. Control of sp^2/sp^3 carbon ratio and surface chemistry of nanodiamond powders by selective oxidation in air. **Journal of the American Chemical Society**, v. 128, n. 35, p. 11635–11642, 2006.

PEIGHAMBARDOUST, S. J.; ROWSHANZAMIR, S.; AMJADI, M. Review of the proton exchange membranes for fuel cell applications. **International Journal of Hydrogen Energy**, v. 35, n. 17, p. 9349–9384, 2010.

RAJA, PAVAN M. V. BARRON, A. R. **Raman Spectroscopy**. Disponível em: <https://chem.libretexts.org/Bookshelves/Analytical_Chemistry/Book%3A_Physical_Methods_in_Chemistry_and_Nano_Science_(Barron)/04%3A_Chemical_Speciation/4.03%3A_Raman_Spectroscopy>.

RALPH, T. R.; HOGARTH, M. P. Catalysis for low temperature fuel cells. **Platinum Metals Review**, v. 46, n. 3, p. 117–135, 2002.

RAMIN, B.; SVOBODA, T. Health of the homeless and climate change. **Journal of Urban Health**, v. 86, n. 4, p. 654–664, 2009.

RHODE, R. **Global Temperature Report for 2019**. Disponível em: <http://berkeleyearth.org/2019-temperatures/>.

ROEN, L. M.; PAIK, C. H.; JARVI, T. D. Electrocatalytic corrosion of carbon support in PEMFC cathodes. **Electrochemical and Solid-State Letters**, v. 7, n. 1, p. A19–A22, 2004.

RYL, J.; BURCZYK, L.; BOGDANOWICZ, R.; SOBASZEK, M. Study on surface termination of boron-doped diamond electrodes under anodic polarization in H_2SO_4 by means of dynamic impedance technique. v. 96, p. 1093-1105, 2016.

SALAZAR-BANDA, G. R.; EGUILUZ, K. I. B.; AVACA, L. A. Boron-doped diamond powder as catalyst support for fuel cell applications. **Electrochemistry Communications**, v. 9, n. 1, p. 59–64, 2007.

SCHNEIDER, P. J. The origin, fate, and health effects of combustion by-products: A research framework. **Environmental Health Perspecties**, v. 59, n. 23, p. 2333–2336, 2002.

SETASUWON, P.; METANAWIN, T. Study of diamond film interface structure and contacting area. **Materials Research**, v. 12, n. 1, p. 89–94, 2009.

SHAFTEL, H.; JACKSON, R.; SUSAN, C.; DANIEL, B. **Overview: Weather, Global Warming and Climate Change**. Disponível em: <https://climate.nasa.gov/resources/global-warming-vs-climate-change/>.

SHARMA, S.; POLLET, B. G. Support materials for PEMFC and DMFC electrocatalysts—A review. **Journal of Power Sources**, v. 208, p. 96–119, 2012.

SHOW, Y.; SWOPE, V. M.; SWAIN, G. M. The effect of the CH_4 level on the morphology, microstructure, phase purity and electrochemical properties of carbon films deposited by microwave-assisted CVD from Ar-rich source gas mixtures. **Diamond and Related Materials**, v. 18, n. 12, p. 1426–1434, 2009.

SHOW, Y.; WITEK, M. A.; SONTHALIA, P.; SWAIN, G. M. Characterization and electrochemical responsiveness of boron-doped nanocrystalline diamond thin-film electrode. **Chemistry of Materials**, v. 15, n. 4, p. 879–888, 2003.

SIMON, N.; GIRARD, H.; BALLUTAUD, D.; GHODBANE, S.; DENEUVILLE, A.; HERLEM, M.; ETCHEBERRY, A. Effect of H and O termination on the charge transfer of moderately boron doped diamond electrodes. **Diamond and Related Materials**, v. 14, n. 3, p. 1179–1182, 2005.

SPIEGEL, C. **Designing and Building Fuel Cells**. New York, NY: McGraw-Hill Education, 2007. v. 87

STEELE, B. C. H.; HEINZEL, A. Materials for fuel-cell technologies. **Nature**, v. 414, n. 6861, p. 345–352, 2001.

STEVENS, D. A.; DAHN, J. R. Thermal degradation of the support in carbon-supported platinum electrocatalysts for PEM fuel cells. **Carbon**, v. 43, n. 1, p. 179–188, 2005.

SWAIN, G. M. The susceptibility to surface corrosion in acidic fluoride media : A comparison of diamond, HOPG, and glassy carbon electrodes. **Journal of the Electrochemical Society**, v. 141, n. 12, p. 3382–3393, 1994.

TASIC, G. S.; MILJANIC, S. S.; MARCETA KANINSKI, M. P.; SAPONJIC, D. P.; NIKOLIC, V. M. Non-noble metal catalyst for a future Pt free PEMFC. **Electrochemistry Communications**, v. 11, n. 11, p. 2097–2100, 2009.

Types of Fuel Cells. Disponível em: <https://www.energy.gov/eere/fuelcells/types-fuel-cells>.

UN 20-year review: earthquakes and tsunamis kill more people while climate change is driving up economic losses. Disponível em: <go.nature.com/2r2jyy6>.

WANG, S.; JIANG, S. P. Prospects of fuel cell technologies. **National Science Review**, v. 4, n. 2, p. 163–166, 2017.

WANG, S.; SWOPE, V. M.; BUTLER, J. E.; FEYGELSON, T.; SWAIN, G. M. The structural and electrochemical properties of boron-doped nanocrystalline diamond thin-film electrodes grown from Ar-rich and H_2-rich source gases. **Diamond and Related Materials**, v. 18, n. 4, p. 669–677, 2009.

WANG, Y.; ZHAO, N.; FANG, B.; LI, H.; BI, X. T.; WANG, H. Carbon-supported Pt-based alloy electrocatalysts for the oxygen reduction reaction in polymer electrolyte membrane fuel cells: particle size, shape, and composition manipulation and their impact to activity. **Chemical Reviews**, v. 115, p. 3433–3467, 2015.

What is Climate Change? Disponível em: <https://www.nps.gov/goga/learn/nature/climate-change-causes.htm>.

WILBERFORCE, T.; ALASWAD, A.; PALUMBO, A.; DASSISTI, M.; OLABI, A. G. Advances in stationary and portable fuel cell applications. **International Journal of Hydrogen Energy**, v. 41, n. 37, p. 16509–16522, 2016.

WILBERFORCE, T.; EL-HASSAN, Z.; KHATIB, F. N.; AL, A.; BAROUTAJI, A.; CARTON, J. G.; OLABI, A. G. Developments of electric cars and fuel cell hydrogen electric cars. **International Journal of Hydrogen Energy**, v. 42, n. 40, p. 25695–25734, 2017.

WILLIAMS, O. A. Nanocrystalline diamond. **Diamond & Related Materials**, v. 20, n. 5–6, p. 621–640, 2011.

WILSON, N. R.; CLEWES, S. L.; NEWTON, M. E.; UNWIN, P. R.; MACPHERSON, J. V. Impact of grain-dependent boron uptake on the electrochemical and electrical properties of polycrystalline boron doped diamond electrodes. **Journal of Physical Chemistry B**, v. 110, n. 11, p. 5639–5646, 2006.

XU, J.; GRANGER, M. C.; CHEN, Q.; STROJEK, J. W.; LISTER, T. E.; SWAIN, G. M. **Boron-Doped Diamond Thin Film Electrodes**. [s.l: s.n.].

YANG, N.; YU, S.; MACPHERSON, J. V.; EINAGA, Y.; ZHAO, H.; ZHAO, G.; SWAIN, G. M.; JIANG, X. Conductive diamond: Synthesis, properties, and electrochemical applications. **Chemical Society Reviews**, v. 48, n. 1, p. 157–204, 2019.

ZANIN, H.; MAY, P. W.; FERMIN, D. J.; PLANA, D.; VIEIRA, S. M. C.; MILNE, W. I.; CORAT, E. J. Porous boron-doped diamond/carbon nanotube electrodes. **ACS Applied Materials & Interfaces**, v. 6, p. 990–995, 2014.

ZAPOL, P.; STERNBERG, M.; CURTISS, L. A.; FRAUENHEIM, T.; GRUEN, D. M. Tight-binding molecular-dynamics simulation of impurities in ultrananocrystalline diamond grain boundaries. **Physical Review B -**

Condensed Matter and Materials Physics, v. 65, p. 454031–4540311, 2002.

ZARAZUA DE RUBENS, G.; NOEL, L.; KESTER, J.; SOVACOOL, B. K. The market case for electric mobility: Investigating electric vehicle business models for mass adoption. **Energy**, v. 194, p. 116841, 2020.

ZENG, H.; KONICEK, A. R.; MOLDOVAN, N.; MANGOLINI, F.; JACOBS, T.; WYLIE, I.; ARUMUGAM, P. U.; SIDDIQUI, S.; CARPICK, R. W.; CARLISLE, J. A. Boron-doped ultrananocrystalline diamond synthesized with an H-rich/Ar-lean gas system. **Carbon**, v. 84, p. 103–117, 2015.

ZHANG, T.; WANG, P.; CHEN, H.; PEI, P. A review of automotive proton exchange membrane fuel cell degradation under start-stop operating condition. **Applied Energy**, v. 223, p. 249–262, 2018.

ZHANG, X.; YANG, Y.; GUO, L.; LIU, H. Effects of carbon corrosion on mass transfer losses in proton exchange membrane fuel cells. **International Journal of Hydrogen Energy**, v. 42, n. 7, p. 4699–4705, 2016.

ZHONG, L.; LEE, C.-S.; HAGHIGHAT, F. Indoor ozone and climate change. **Sustainable Cities and Society**, v. 28, p. 466–472, 2017.